Wind retrieval from synthetic aperture radar - an overview

Dagestad, Knut-Frode ; Horstmann, Jochen ; Mouche, Alexis ; Perrie, William ; Shen, Hui ; Zhang, Biao ; Li, Xiaofeng ; Monaldo, Frank ; Pichel, William; Lehner, Susanne

Total number of authors:
17

Published in:
Proceedings of SEASAR 2012

Publication date:
2013

Document Version
Publisher's PDF, also known as Version of record

WIND RETRIEVAL FROM SYNTHETIC APERTURE RADAR – AN OVERVIEW

Knut-Frode Dagestad[1,2], Jochen Horstmann [3], Alexis Mouche[4], William Perrie[5], Hui Shen[6], Biao Zhang[7], Xiaofeng Li[8], Frank Monaldo[8,9], William Pichel[8], Susanne Lehner[10], Merete Badger[11], Charlotte Bay Hasager[11], Birgitte Furevik[12], Ralph C. Foster[13], Silvia Falchetti[3], Michael J. Caruso[14], Paris Vachon[15]

[1] Nansen Environmental and Remote Sensing Center, Thormohlens gt 47, N-5006 Bergen, Norway
[2] StormGeo AS, Nedre Nøstegaten 1, N-5011 Bergen, Norway, Email: kfd@stormgeo.com
[3] Centre for Maritime Research and Experimentation, NATO Science and Technology Organization Viale San Bartolomeo 400, 19126 La Spezia, Italy, Email: horstmann@cmre.nato.int, falchetti@cmre.nato.int
[4]CLS, Radar Applications, Technopôle Brest-Iroise, 29280 Plouzane, France, Email: amouche@cls.fr
[5] Bedford Institute of Oceanography, Fisheries and Oceans, Canada, B2Y 4A2, Email: william.perrie@dfo-mpo.gc.ca
[6] Institute of Oceanology, Chinese Academy of Sciences, 7 Nanhai Rd, Qingdao, China, Email: shenhui@qdio.ac.cn
[7] Nanjing University of Information Science and Technology, School of Marine Sciences, 219 Ningliu Road, Nanjing, 210044, China, Email: zhangbiao@nuist.edu.cn
[8]NOAA Center for Weather and Climate Prediction, NOAA/NESDIS/STAR, 5830 University Research Court, College Park, MD 20740 U.S.A., Email: xiaofeng.li@noaa.gov, William.G.Pichel@noaa.gov
[9]Johns Hopkins University Applied Physics Laboratory, Space Department, 11100 Johns Hopkins Road, Laurel, MD 20723, USA, Email: frank.monaldo@jhuapl.edu
[10]German Aerospace Center (DLR), Oberpfaffenhofen, D-82234 Wessling, Germany, Email: Susanne.Lehner@dlr.de
[11]Technical University of Denmark, Department of Wind Energy, DTU Risø Campus, Frederiksborgvej 399, 4000 Roskilde, Denmark, Email: mebc@dtu.dk, cbha@dtu.dk
[12]Norwegian Meteorological Institute, Allégaten 70, 5007 Bergen, Norway, Email: birgitte.furevik@met.no
[13]Applied Physics Laboratory, University of Washington, 1013 NE 40th St., Seattle, Washington, USA, Email: ralph@apl.washington.edu
[14]Center for Southeastern Tropical Advanced Remote Sensing, University of Miami, 11811 SW 168TH Street, Miami, FL 33177, USA, Email: mcaruso@rsmas.miami.edu
[15]Radar Applications and Space Technologies, Defence R&D Canada, 3701 Carling Ave. Ottawa, ON, Canada K1A 0Z4, Email: Paris.Vachon@drdc-rddc.gc.ca

ABSTRACT

This paper represents a consensus on the state-of-the-art in wind retrieval using synthetic aperture radar (SAR), after the SEASAR 2012 workshop "Advances in SAR Oceanography" hosted by the European Space Agency (ESA) and the Norwegian Space Centre in Tromsø, Norway 18–22 June 2012. We document the recent advances of the methodologies, which are capitalizing on the improved capabilities of the modern generation of SAR sensors providing Doppler grid and multi-polarizations. The many applications of SAR wind retrieval have also benefitted from on the improved availability of wide swath modes (~500 km) with excellent coverage, giving much better overview of regional and mesoscale wind features. The accuracy of offshore wind retrieval is robust and generally in the order of 1.5 m/s in speed and 20° in direction, whereas the new methodologies steadily improve the performance for the more challenging conditions near cyclones and complex coastal topography.

1. INTRODUCTION

Synthetic Aperture Radar (SAR) is a unique resource to measure wind over water surfaces at a spatial resolution of a few hundred meters. The measurement principle is similar to scatterometers, but the improved spatial resolution of SAR allows monitoring a wide range of mesoscale processes not resolved by scatterometers with their resolution of the order of 10 kilometers. The higher resolution further allows monitoring of wind close to the coastlines, where most of the human offshore activities are confined. The drawback of SAR is the poorer temporal coverage due to more narrow swaths, but this has improved significantly over the last decade with more sensors with wider swaths of 400-500 kilometers, compared to typically 100 kilometers for the first generation sensors.

Nearly 25 years since its infancy with the SEASAT satellite launched in 1978, the application of SAR for wind retrieval has become mature. Yet several improvements and new methodologies have been seen in recent years, partly capitalising on improved sensors with several operating modes (see Table 1). A thorough overview of the history of using SAR for wind retrieval is given in the whitepaper from the SeaSAR workshop in Spitzbergen in 2003 [1]. The present paper will highlight what is new since then, still aiming to give a complete, yet brief, overview of the current state-of-the-art.

Proc. of 'SEASAR 2012', Tromsø, Norway
ESA SP-709, January 2013

Traditionally, SAR wind retrieval has been based on a single observed quantity; the co-polarized Normalized Radar Cross Section (NRCS). Within the last decade it has been demonstrated that two other types of resources are also useful for wind retrieval: cross-polarized NRCS and the Doppler Centroid Anomaly. Section 2 describes these resources, and their theoretical and empirical relationship to the near surface wind. In Section 3 we show some examples of how these fundamental relationships are used and combined for practical retrieval of the ocean wind fields. In Section 4 we show examples of several applications of SAR wind, and in Section 5 we discuss the future outlook.

2. FUNDAMENTAL RELATIONSHIPS BETWEEN SAR OBSERVABLES AND WIND

2.1. The SAR observables

Synthetic Aperture Radars transmit coherent microwaves that are either vertically (V) or horizontally (H) polarized, and form images of the NRCS (σ_0) by recording the backscattered signal in either of the polarizations. If the same polarization is used for both transmitting and receiving, the images are co-polarized (VV or HH); otherwise the images are cross-polarized (VH or HV). Some modern and future SAR systems (Table 1) may transmit and submit in both polarizations alternately, and hence provide up to four concurrent SAR images (observables). As discussed in Section 2.3, it has been found that co-polarized and cross-polarized NRCS have qualitatively different relationships with the wind. Besides using different polarizations, SAR sensors have different wavelengths in the range of 2-30 cm (Table 1), which has been found to only make a quantitative difference; the principles remain the same. Examples of co-polarized and cross-polarized NRCS images from the same SAR scene are shown in Figure 1.

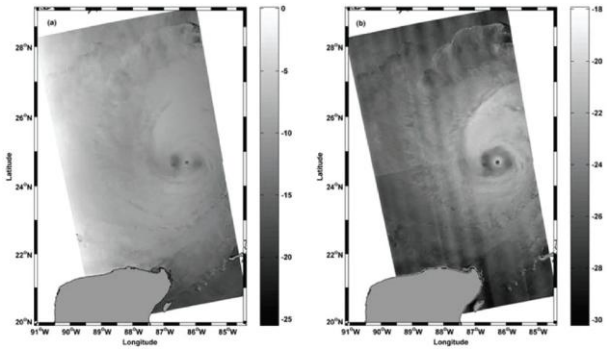

Figure 1: Illustration of VV polarized (left) and VH polarized (right) NRCS from a RADARSAT-2 dual-polarization scene acquired over Hurricane Ike at 2356 UTC 10 Sep 2008. RADARSAT-2 data and product from MacDonald, Dettwiler and Associates Ltd. Figure from Ref [60].

In addition to the NRCS images, the Doppler Centroid anomaly is another resource available from SAR imagery. A median ("Centroid") Doppler shift is calculated from the azimuthal gradient of the phase of the return signal, and is used to provide high resolution (~10-100 m) of the NRCS, despite antenna footprint sizes of the order of 5 kilometers. The main contribution to the Doppler Centroid is due to the relative motion of the satellite and the surface of the rotating Earth, but the anomaly obtained by predicting and subtracting this part is found to be a useful measure of the radial (line of sight) component of the velocity of the (ocean) surface, which is related to both wind, waves and currents [2], [3], [4]. The Doppler Centroid anomaly is typically obtained with pixel sizes of the order of 5 km (similar to antenna footprint), where accuracy can be traded versus spatial resolution. A Doppler velocity is calculated from the Doppler shift with the standard Doppler relation [3]. A Doppler Centroid grid will be provided with future Sentinel-1 products, as it was for Envisat ASAR wide swath products, but can be calculated from any Single Look Complex SAR images using e.g. the method from [5].

Despite the complex retrieval methods, the Doppler Centroid anomaly can be interpreted simply as a NRCS-weighted Doppler shift from the moving ocean surface, as could also have been retrieved from real aperture radars, including non-moving sensors.

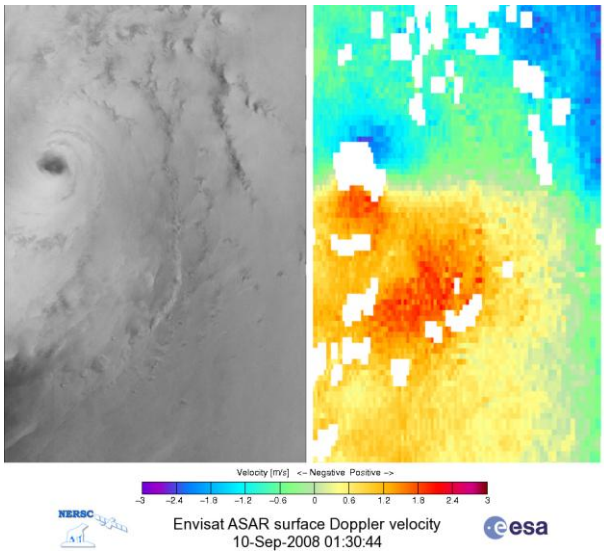

Figure 2: Envisat ASAR VV NRCS image (left) with corresponding Doppler velocity (right) acquired over Hurricane Ike at 0130 UTC 10 Sep 2008. The colorbar refers to the Doppler image, with positive (negative) values indicating motion towards right (left).

2.1.1. Wind direction from NRCS wind streaks

Though not a direct SAR observable, the direction of the wind (with an ambiguity of 180 degrees) can be obtained from streak-like features visible in NRCS images. Atmospheric roll vortices induces lines of increased and decreased near surface winds, which, in turn produce lines of increased surface roughness, and hence SAR NRCS. Also elongated convective cells, wind-driven Langmuir cells, or the distribution of wind-distributed surfactants may lead to visible streaks aligned along the wind direction. [6], [7].

Wind direction may be obtained from the streaks using Fourier transforms detecting features at scales of 600 m to about 2 km [8], [9], [10]. Other approaches include wavelet analysis [11], [12], estimating local gradients on different spatial scales [13], [14], [15], [16], and detecting the direction of the largest variance [17], [18]. All of these methods lead to a 180 degree ambiguity, which can be resolved either by comparing with models, detecting land shadows [9], or by using Doppler shift [4]. The accuracy of various algorithms is in the range of 15-40 degrees [7].

2.2. Physical models

Physical modelling of the relationship between the SAR observables and near surface wind speed requires solving two independent problems:

1. Determination of the ocean surface wave spectrum based on wind speed and other geophysical parameters.
2. Calculation of the electromagnetic signals received by the SAR from the ocean surface for the given wave spectrum and satellite configuration.

The wave spectrum calculated in the first step must be directional (2D) in order to take into account various SAR look directions in the second step, and its accuracy around the radar wavelength (~2-20 cm) is of particular importance. In the simplest case, the wave spectrum can be determined by semi-empirical models taking as input only the wind speed and eventually wave-age (steepness), such as the widely used model of [19]. A more advanced physical model for the wave spectrum is used by [20], allowing investigation of the sensitivity to atmospheric stability, water temperature/viscosity and surface dampening coefficients, as well as the spatial variations of the same parameters.

Calculation of the electromagnetic signals in the second step takes into account the radar wavelength and polarization, and the incidence angle and azimuth sensor look direction (relative to the wind direction). Empirical and semi-analytical expressions tuned to laboratory and *in situ* measurements are used for the contributions from various scattering mechanisms such as specular ("mirror") scattering and resonant Bragg scattering [21], [22], [23], as well as scattering from the more ill-behaved water surface associated with breaking waves [24], [20]. Most scattering models are based on a two-scale decomposition [25] of the wave spectrum, where the shorter resonant Bragg waves are tilted and modulated by the longer waves on meter scales [26]. Recent studies [27], [28] have demonstrated the importance of the sea surface curvature (second derivative of the wave elevation spectrum).

The Doppler shift can be calculated from the cross-correlation of the (orbital) speed of the surface (along the radar look direction) and the corresponding local NRCS for the given polarization [28], [29], [30], [31]. It is thus a weighted surface velocity, which in simple terms is generally positive in the direction of the wind since the forward moving facets of the orbital wind waves have higher NRCS than the backwards moving facets.

Although the models can give fair agreement with the SAR observables (e.g. [20], [28], [32]), the empirical relationships of Section 2.3 have rather been used in practice for wind retrieval (Section 3), as these are both faster and simpler to operate, and show the best agreement with the observations (to which they are tuned). The physical models are nevertheless invaluable for advancing the understanding of the involved physical processes, and for the design of future sensors. Two widely used radar imaging models are the M4S software by Roland Romeiser and the DopRIM model of Vladimir Kudryavtsev.

2.3. Empirical relationships

A function which relates the radar observables (NRCS or Doppler) to the near surface wind is called a Geophysical Model Function (GMF). Below we give an overview of some empirical GMFs for co-polarized NRCS, cross-polarized NRCS and Doppler shift.

2.3.1. Co-polarized NRCS (VV, HH)

The GMF that was developed by ESA for the C-band scatterometer onboard the ERS-satellites is called CMOD (C-band MODel) [33], [34]. The fourth version of this model, CMOD4 [35], [36], was developed by empirically fitting the VV-polarized NRCS measurements from ERS-1 to ECMWF analysis winds, and was used for the official ERS scatterometer products since 1993. Although developed with scatterometer measurements, the GMF is applicable to any measurements of VV-polarized C-band NRCS, including SAR with its much higher resolution [37]. As with all other empirical GMFs for co-polarized

radiation, NRCS is a function of three parameters: the SAR incidence angle, wind speed, and wind direction relative to the SAR look azimuth direction.

At high wind speeds, CMOD4 was found to overestimate NRCS, leading to too low retrieved winds [38], [39]. Overestimation of the upwind-downwind asymmetry and upwind-crosswind term further had some impact the quality of ambiguity removal and wind direction for the scatterometry algorithms, though minor impact on the retrieved wind speed. An updated version, CMOD5 [40], was tuned to 22 million ERS-2 NRCS and ECMWF wind collocations, using additional aircraft measurements of extreme backscatter with accompanying *in situ* wind observations for improved performance for higher wind speeds. CMOD5 also reduced some known incidence angle biases of CMOD4. Another GMF (CMOD_IFR2) was developed independently at Ifremer, also with particular focus on the higher wind speeds [41].

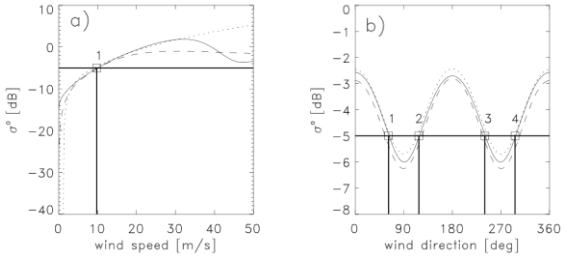

Figure 3: Comparison of the C-band GMFs CMOD4 (dotted line), CMOD5 (dashed line) and CMOD-IFR2 (thin solid line) at incidence angle of 25 degrees. The horizontal thick line corresponds to a -5dB backscatter value; vertical thick lines correspond to SAR-wind solutions for (a) wind speed (one solution) and (b) wind direction (up to four solutions). Figure from Ref. [42].

As the above GMFs are tuned to actual (model) winds at 10 m height, they are valid for the average near surface stability, which is not neutral. An updated version of CMOD5 (CMOD5.N) was developed by [43] to provide 10 m winds at neutral conditions, making it simpler to avoid errors related to atmospheric stratification [44]. In addition to an average stability compensation of 0.2 m/s, CMOD5.N also adds 0.5 m/s to compensate for an overall low bias of CMOD5 [45].

In 1995, when RADARSAT-1, the first SAR operating in HH co-polarization at C-band was launched, there was no existing GMF for this polarization. Also, as no scatterometer has ever been launched in HH, there was no way to rely on the experience from scatterometry. Because of the lack of data [46] proposed to circumvent the question of the GMF by introducing the polarization ratio (PR). The idea was to convert the signal measured in HH into VV polarization before using a GMF from the CMOD family. A simple empirical formula was proposed:

$$PR \equiv \frac{\sigma_0^{VV}}{\sigma_0^{HH}} = \frac{(1 + 2\tan^2\theta)^2}{(1 + \alpha\tan^2\theta)^2}, \qquad (1)$$

where α is a parameter relating the type of surface scattering. Several values were proposed for α [1], but the initial value proposed by [46] was 0.6. This debate around the value is closely related to the calibration of the considered sensor and to the sea surface conditions we are interested in. Indeed, this parameterization is far too simple as both theories based on asymptotic solutions [47], [28] and new measurements indicate that the PR is wind speed [48] and wind direction dependent [49]. Beyond this debate, the PR turned out to be meaningful information to evaluate the relative weight of the different scattering mechanisms involved in the scattering [20], [50].

Since ENVISAT and RADARSAT-2 missions, the number of SAR acquisition has significantly increased. Thus, there may no longer be a need to keep relying on the scatterometers in order to define the GMF for SAR. Based on massive triple co-locations between wind given by ECMWF, ASCAT and NRCS measured from ASAR, [83] show how the SAR measurement could be used to derive the coefficients of a GMF in both VV and HH. As expected the results are very close to CMOD-5 in VV and HH NRCS is less saturated for high winds. Results of this GMF in HH are shown in Figure 4. This has also been done for Doppler in VV and HH [4] and for the NRCS in cross-polarization [60].

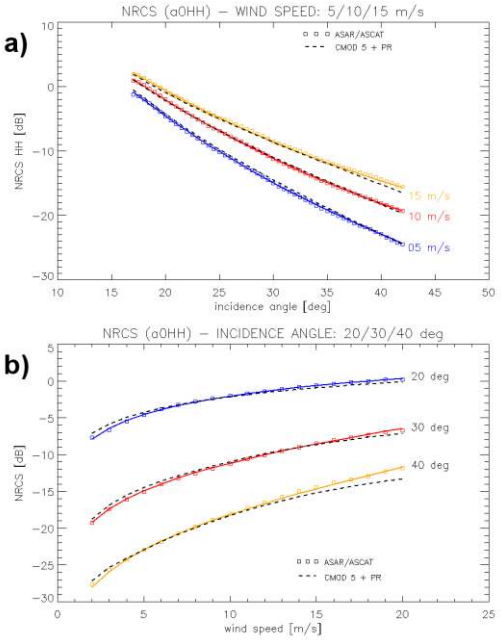

Figure 4: (a) NRCS as a function of incidence angle for 5, 10 and 15 m/s wind speeds. (b) NRCS as a function of wind speed for 20, 30 and 40° incidence angle. Colored squared are NRCS from ASAR, dottes line is CMOD 5 combined with PR from [49] and colored line is the result of the GMF.

Launch of the X-band (3.1 cm wavelength) German TerraSAR-X and Italian COSMO-SkyMed SAR satellites in 2007 stimulated the need and interest to develop GMFs for X-band. An empirical GMF developed for airborne X-band VV scatterometer data [51] was found unsuitable for SAR wind retrieval by [52], who developed a linear GMF (XMOD1) by collocating SIR-X-SAR (Endeavour space shuttle) with ERA-40 reanalysis wind speeds. A non-linear GMF (XMOD2) was also developed at DLR by co-locating TerraSAR-X measurements with in situ buoy wind speeds [53]. A challenge when developing X-band GMFs is the limited datasets currently available. Therefore a different approach was applied by [32], who developed an X-band GMF by interpolating the coefficients of well-tested C-band (5.7 cm) and Ku-band (2.2 cm) GMFs.

Wind features were clearly visible in early L-band images from SEASAT (which operated in 1978 until it failed after only 105 days), but the SAR instrument was not sufficiently well calibrated for quantitative retrieval of wind [8], [53]. Two L-band SAR-sensors have later been launched by the Japan Aerospace Exploration Agency (JAXA). A GMF for L-band HH polarization was developed by [56] for the JERS-1 SAR. An updated version, also for HH polarization, was developed by [57] by co-locating ALOS PALSAR NRCS measurements with scatterometer wind vectors. Due to the longer radar wavelength (23.6 cm for PALSAR), this GMF is less sensitive to winds than C-band GMFs at moderate winds and large incidence angles, whereas it is comparable at winds above 10 m/s and small incidence angles. An anticipated advantage of L-band is to avoid the saturation of NRCS for winds above 20 m/s which is seen for X- and C-band. This could however not be verified by [57], due to limited number of co-locations at high winds.

2.3.2. Cross-polarized NRCS (VH, HV)

With the launch of the Canadian satellite RADARSAT-2, a large dataset of cross-polarized SAR images has been accumulated by researchers. By collocating SAR imagery with National Data Buoy Center (NDBC) buoys off the east and west coasts of North America, which have provided measured *in situ* winds, the relationships between cross-polarized NRCS and wind speed, direction and radar geometry has been established [58], [59], [60], [61]. Thus, it was shown that cross-polarized SAR returns have no dependence on radar incident angle and wind direction. This remarkable characteristic embodied by the unique proportional relationship with only wind speed makes the cross-polarized SAR image mode optimal for wind speed retrievals and operational marine wind monitoring. Thus, wind speed can be retrieved from cross-polarized SAR images directly without the need for external wind direction information. Therefore, cross-polarized SAR mode imagery is especially valuable for observations of wind fields in situations where rapid wind directions occur, such as tropical cyclones.

For cross-polarized SAR imagery, the state-of-the-art for the geophysical model function (GMF) is the C-2PO (C-band Cross-Polarized Ocean) model [60], which exhibits a distinctly linear relationship between the NRCS and wind speed. The C-2PO model relates the cross-pol NRCS to wind speed at 10-m height (U_{10}) according to

$$\sigma^{o}_{VH} = 0.580 * U_{10} - 35.652 \qquad (2)$$

Here, the units of σ^{o}_{VH} and U_{10} are dB and m/s, and an example of the data on which C-2PO is based is given in Figure 5. The observed NRCS in cross-pol mode increases linearly with wind speed, up to 26 m/s. The relation shows no indication of saturation or ambiguity, which is a problem for high wind speed retrievals using co-polarized NRCS [63], [64].

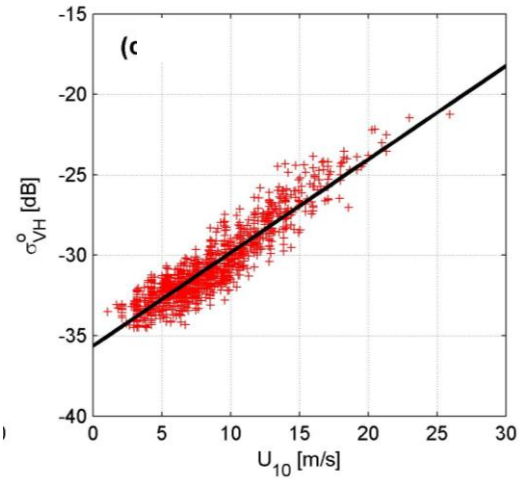

Figure 5: Mean cross-pol NRCS, σ^{o}_{VH}, versus *in situ* buoy observed wind speed at 10-m height, U_{10}. The solid line corresponds to a nonlinear least square fit, with a correlation coefficient of 0.91 with Eq. (2).

However, for SAR data acquired with Radarsat-2 in the ScanSAR mode this relation looses validity due to the different settings of the SAR sensor, which leads to sensor artefacts such as cross talk between the channels as well as contribution of the noise floor to the NRCS, which have to be considered in the processing at such noise floor levels. Due to the cross talk issue, which can be corrected for in the quadpol data used above, a dedicated GMF has been developed, which compensates for these artefacts [61].

2.3.3. Doppler shift

The correlation between wind speed from the ECMWF model (projected into the SAR look direction) and Doppler Centroid anomaly from Envisat ASAR Wave Mode (incidence angle of 23°) was demonstrated at the SeaSAR workshop in Spitzbergen in 2003 [1], and several studies have been published to explain this measure. In the absence of an underlying sea surface current, the Doppler shift induced by the near surface wind is interpreted as the mean line-of-sight velocity of the radar detected scatter elements [2]. Considering the Bragg mechanism, the velocity of these roughness elements is fixed and related to their phase velocity. However, as tilted by longer waves, the NRCS varies along these wave profiles, leading to correlation with horizontal and vertical orbital velocities. Consequently, the Doppler shift is first strongly dependent upon the strength of the tilt modulation [25]. Thus, as for the NRCS, the resulting Doppler is a combination of the relative weight of the smallest and slowest waves (Bragg) contributing with respect to the largest and fastest (tilting) waves that depends on incidence angle, polarization and frequency [29].

After the Doppler Grid was made available by ESA in ASAR wide swath imagery since 2007, a full GMF (called CDOP) could be developed by [4] by co-locating the Doppler anomalies with ASCAT scatterometer winds. It was demonstrated that the Doppler Centroid anomaly shows dependency on the same parameters as the co-polarized NRCS; namely the incidence angle, wind speed, and wind direction relative to the SAR look azimuth direction. CDOP was developed for both HH- and VV-polarization, where an example plot of the latter is seen in Figure 6.

As shown by [4], the great benefit of using the Doppler shift is its unique wind direction dependency. This makes this quantity very valuable to better constrain the wind inversion and resolve the issues regarding the wind direction in cases of complex systems such as atmospheric fronts or low pressure systems. Though fitted to Doppler Centroid anomalies from Envisat ASAR, the CDOP function should be valid for any measurements of the C-band Doppler shift from the sea surface, including regular Doppler shift from a Real Aperture Radar. An ongoing ESA pilot project (DOPSCAT) investigates the potential of utilizing Doppler shift from scatterometers.

It is important to note that the Doppler shift also contains a contribution from the radial ocean surface current, as well as from the interaction between waves and currents [29]. Thus unless the current is negligible or directed along the azimuth direction, this component should be taken into account when retrieving wind. As a matter of fact, Doppler shift has already been used to study large and steady currents such as the equatorial currents [66] or the Agulhas current [67] after the removal of the wind contribution. In these works, the methodology relies on the hypothesis that at relatively low resolution (typically greater than 5 km), the averaged interactions between current and wind are negligible in the measured Doppler anomaly. Following this assumption wind and currents effects can be considered as additive. When dealing with higher resolution, this hypothesis is not valid anymore. In these cases, the methodology to separate wind, waves and current contributions has still to be developed and will need to involve physically-based models [29], [30].

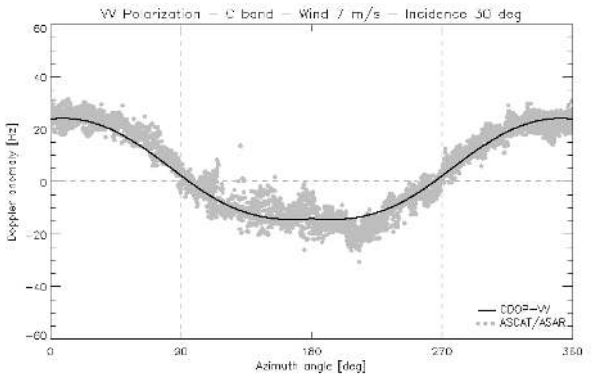

Figure 6: Envisat ASAR Doppler Centroid anomaly for VV polarization plotted versus azimuth angle (SAR look versus wind direction) for ASCAT wind speeds of 7 m/s and incidence angle of 30 degrees. The solid line is the CDOP GMF fitted to the measurements.

2.4. The near-surface wind speed

By convention, the physical and empirical models discussed above relate the NRCS and Doppler shift to the wind speed at 10 meter height above the sea surface. These relations are indirect, as the ocean surface roughness is generated by the wind stress and momentum transfer at the very ocean-air interface (expressed as the "friction velocity"), rather than the wind at 10 meter height. Careful laboratory and *in situ* measurements have indeed confirmed that the NRCS shows a closer relationship with the friction velocity than with the wind at any particular reference height [8], [68]. Nevertheless, *directly* relating the SAR observables to the wind at 10 meter is a more practical solution, as this is a more useful quantity than friction velocity for most end users. Furthermore, the relation between friction velocity and wind at any reference height depends on detailed information about the near-surface stability, which is generally not available over the ocean. Post-processing corrections can be applied if information on the near surface stability can be obtained from a forecasting model, from buoy measurements, or from the fine-scale variability of the NRCS (e.g. [69]).

3. WIND INVERSION

Inversion of the wind from SAR observables is a non-trivial exercise, despite the existence of the empirical relationships discussed in Section 2.3. The simple reason is that wind is a vector quantity (speed and direction, or U- and V-components); hence using any single observed scalar quantity leads to an underdetermined problem. The solution is either to use complementary information from other sources, or to combine several SAR observables. Below we give several examples of how this has been done in practice.

3.1. Examples of wind inversion schemes

3.1.1. Classical scheme using co-pol data

The most common method for SAR wind retrieval has been to combine co-polarized (VV or HH) NRCS-images and complementary information on the wind direction as input to any of the empirical GMFs of Section 2.3.1. The simplest is to take wind direction from a numerical forecast model, such as ECMWF, NCEP GFS or WRF. This works generally well where wind direction gradients are smooth, but is less satisfactory near strong wind direction gradients such as fronts and cyclones, where models are too coarse, or may have the wind gradient features shifted in time and/or space. A well known example is the "hourglass effect" which arises if a cyclone centre of the model wind direction is only slightly displaced from the SAR cyclone centre. Taking wind directions from scatterometer measurements can work better if such measurements are available close in time, ideally within less than one hour. Taking wind directions from wind streaks of the given SAR image has the advantage of no time-difference, but such streaks may not always be clearly visible (Section 2.1.1). The 180 degree ambiguity may be resolved by complementary model or Doppler data, but again the spatial resolution may be a limiting factor. Only wind speed is output from this classical scheme, as the wind direction is merely an input parameter. This may however be reversed by taking the wind speed from a model or scatterometer to invert wind direction, though this may lead to ambiguities.

For wind fields that do not change abruptly, the wind speed can be retrieved from RADARSAT-1 SAR imagery by making the assumption that the winds in two neighbouring sub-image blocks are essentially the same [70]. This approach is taking the concept of wind retrieval from scatterometer imagery, where there is more than one measurement for each element of ocean surface. Thus, assuming simple Holland-vortex hurricane spatial structure, hurricane wind speeds could be retrieved without invoking external wind direction information from other sources [71].

3.1.2. Using cross-pol data only

As discussed in Section 2.3.2, cross-polarized NRCS is simply proportional to wind speed, with no dependency on wind direction or incidence angle. Thus, the wind speed can be directly obtained from cross-pol SAR images without complementary external information.

In Hurricane Earl, direct high wind speed (>20 m/s) comparisons between spaceborne SAR retrievals and airborne SFMR measurements show that bias and RMS error for derived wind speeds from C-2PO are -0.89 m/s and 3.23 m/s respectively, whereas for CMOD5.N these numbers are -4.14 m/s and 6.24 m/s. But models underestimate high winds (30~38 m/s), possibly because: 1) CMOD5.N is then saturated, 2) co- and cross-pol NRCS calibration error, 3) CMOD5.N and C-2PO do not account for the rain contamination and effects of high waves.

Figure 7 shows the wind fields of Hurricane Earl (a category 2 storm at the time of acquisition) retrieved from the VV and VH NRCS from RADARSAT-2 ScanSAR mode using the algorithm from [61]. Comparison of the SAR wind speeds to SFMR wind speeds (superimposed) clearly show a much better agreement for the cross pol data in particular at the very high wind speeds. Also the typical 'hour glass effect' observed in co-pol data is not observed in cross pol retrieved winds. Furthermore, the GMF of cross pol data does not show saturation effects of the NRCS at high wind speeds. However, at low wind speeds (<10 m/s) cross pol data are strongly biased by the noise floor such that they cannot be used for wind speed retrieval.

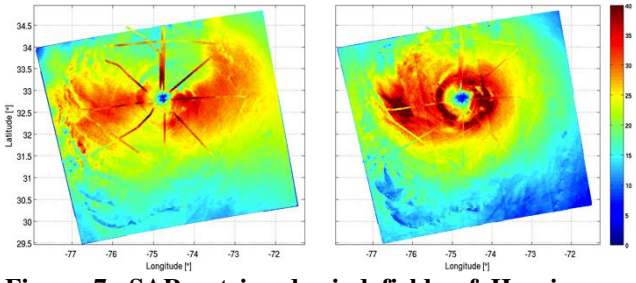

Figure 7: SAR retrieved wind fields of Hurricane Earl acquired on 2 September 2010 at 22:59 UTC at VV pol (left hand side) and VH pol (right hand side). For comparison the wind speed results from the SFMR flights are superimposed to the SAR retrieved winds. The color scales represent wind speeds in m/s.

3.1.3. Using dual polarization data

Because of the ability of RADARSAT-2 of measuring in both cross and co-polarization, new methods emerge to rely on both VH and HH for wind estimate. Ref. [75] produced an "inverse GMF" which relates directly the wind speed to the incidence angle, the normalized radar

cross section in VH and HH with respect to the wind direction relative to the azimuth look angle.

3.1.4. Quad-pol method

Recently, a methodology was presented [76] to simultaneously retrieve wind speed and direction based on RADARSAT-2 fine quad-pol mode single SAR data. Specifically, C-2PO and NRCS data in VH polarization are used to directly retrieve the wind speed without any external wind direction and radar incidence angle inputs. Then the resulting wind speeds from C-2PO and NRCS in VV polarization, and incidence angles are passed to CMOD5.N to estimate the wind direction, with ambiguities. However, the co-pol backscatters have *even* symmetry with respect to the wind direction, while the polarization correlation coefficient (PCC) between the co- and cross-pol channels has *odd* symmetry, with respect to the wind direction. This symmetry property allows removal of wind direction ambiguities. Ref. [76] presents three cases to show that it is feasible to derive ocean surface vector wind images using this method.

3.1.5. Statistical inversion

The first statistical SAR wind algorithm was proposed by [77], who used Bayesian statistics to derive a cost-function to retrieve the optimal wind field from SAR NRCS and model wind vectors (HIRLAM). This approach acknowledges that all sources of information contain errors, and has the advantage that not only wind speed but also wind direction is an output of the algorithm. The same approach was applied by [4] who combined Envisat ASAR Doppler Centroid and NRCS with model wind vectors. As such it should enable the combination of NRCS, Doppler or any other feature derived from the SAR image analysis (e.g. wind direction from streaks signature) taking benefit of all the polarization possibilities of new and forthcoming sensors.

3.1.6. Using atm. pressure gradients

Most SAR wind retrieval methods solve for the wind vector at each pixel largely independently of neighbouring pixels. However, the surface winds are not arbitrary and independent; they are determined by the atmospheric dynamics. An alternative method for SAR wind retrieval thus consists in seeking an integral property of the wind vector field as a means of imposing scene-wide consistency in the retrieved ocean vector winds.

The pressure gradient force is a dominant term in the planetary boundary layer (PBL) momentum budget. Consequently, the imprint of the surface stress field can be used to estimate the surface pressure gradient field through the use of a diagnostic PBL model. In its simplest form, the standard PBL model assumes that the mean advective forces are relatively small and that the flow is neutrally-stratified and barotropic. The standard PBL model includes the effects of thermal winds, boundary layer stratification, a gradient wind correction for curved flow and momentum entrainment across the boundary layer top.

In tropical cyclones, the nonlinear momentum terms are of leading order, comparable to the pressure gradient forcing. Furthermore, the swirling flow in the boundary layer causes the boundary layer to become shallower closer to the center of circulation. Consequently, for tropical cyclones, the nonlinear dynamics are modified to include a strong gradient wind correction to parameterize the first-order nonlinear dynamics and the Rayleigh discriminant of the rotational flow is used to scale the boundary layer depth as in [72].

Scene-wide wind vector retrieval is at least a two-step process. An initial guess wind vector field is obtained using standard methods and is used as an input to the PBL model. For each surface wind vector, a corresponding estimate of the pressure gradient vector is calculated. These pressure gradient vectors have inherent error due to errors in the surface wind inputs and the PBL model. However, we use these vectors as input to a least-squares method to find the optimal sea-level pressure pattern corresponding to the input surface wind vector field. Due to the dynamical constraints imposed by the PBL model, the effects of local errors in the surface wind vectors or relatively large regions of missing vectors are mitigated.

The derived SLP patterns may be used as inputs to the PBL model to re-derive an “SLP-filtered” surface wind field. This product is the scene-wide estimate of the surface wind vectors. The overall method and the high quality of the SLP fields and derived wind vectors using QuikSCAT and ASCAT scatterometer wind vector data has been extensively documented in several papers [73], [74]. We find that both the SLP-filtered wind speeds and directions are modified from the input vectors. Another important aspect of the SLP-filtered wind vectors is that reasonable gradient fields can be calculated.

An example of this method applied to Typhoon Malakas (2010) is shown in Figure 8. The SLP-filtered winds have improved the “hourglass” wind speed errors in the cross-beam regions of the inner-core of the typhoon.

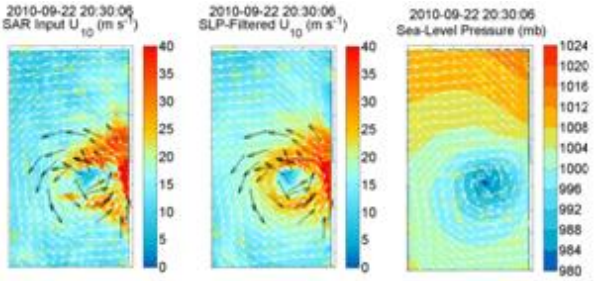

Figure 8: SAR image of Typhoon Malakas, 22 Sep, 2010, 20:30. Left, raw SAR winds, Center: SLP-filtered winds; Right: derived SLP field. The winds are calculated for 1 km pixels. The white arrows are all the same length and show the SAR wind directions every 30 km

An important aspect of this methodology is the use of surface pressure measurements as a means of calibrating and validating the SAR wind vectors. Even without using ancillary data to set the absolute value of the pressure field, the bulk pressure gradient (BPG) between any two points in the SAR-derived pressure field is the optimal estimate of that pressure difference derived from the input SAR winds. Because pressure is an integral property of the winds, pressure differences are more useful than point-by-point wind vector comparisons for assessing the quality of surface wind retrievals because the BPGs characterize the accuracy of a swath of wind vectors (speed and direction) largely in the neighborhood of the pressure measurements.

3.2. Validation numbers

SAR winds may be validated against in situ measurements (e.g. buoys), and scatterometer and model winds. For most studies a bias smaller than 0.5 m/s is found, with standard deviations typically between 1.2 and 2.0 m/s [4], [14], [32], [37], [52], [56], [57], [58], [60], [61], [63], [64], [65], [70], [71], [72], [77], [78], [79], [83], [85], [93], [94], [149]. Algorithms which retrieve wind direction typically report a standard deviation of 15°-40° for the direction [80]. The validation numbers depend on the spatial averaging of the SAR NRCS, the temporal averaging of the in situ measurements, and the time difference. The accuracy decreases in vicinity of strong wind direction gradients, such as in cyclones. The difference between SAR winds and scatterometer and model winds is found to increase markedly for co-locations within 100 km of the coastline, most likely due to degraded performance of the scatterometers and models [78], [79]. Calibration errors will have a larger impact on wind retrievals at low incidence angle and high wind speed (> 20m/s).

3.3. Preprocessing and postprocessing

Whichever algorithm is used to retrieve winds, some pre- and postprocessing of the data is needed to ensure a high quality end product.

- SAR data are often disseminated uncalibrated by space agencies, to reduce file sizes or to facilitate recalibration with updated coefficients. Hence the first step in calculating SAR wind is normally to apply calibration coefficients provided with the SAR product or separately. The calibration accuracy should not exceed 0.5 dB [84].
- Scalloping is an artefact of ScanSAR imagery due to inaccurate estimation of Doppler Centroid, leading to dark and bright stripes along range direction. This may lead to small biases of wind speed, and may confuse wind streak direction algorithms. Methods to correct for scalloping are given in [81] and [82].
- The calibrated NRCS may include instrumental noise, which may lead to wind speed biases of 0.5 m/s or more for larger incidence angles, and should be removed [83].
- Though wind may in principle be retrieved from SAR at full spatial resolution (~5-150 meters), the finest scale NRCS variability is mainly due to speckle, in particular for Single Look Complex imagery. Common practice is to blockaverage the NRCS to 500 m or 1000 m pixel size before wind retrieval. Care should be taken so that no bright targets from land or ships are included when averaging.
- Land and sea ice should be masked in the end product. Whereas high resolution land masks are suitable, obtaining a high resolution ice-mask is more of a challenge [14].
- Volume scattering from rain in the atmosphere may also give a significant bias for shorter wavelengths (X-band), and even for C-band in the case of extreme precipitation (e.g. hurricanes).
- For some users, an error estimate for the wind is needed, e.g. when used as input to statistical algorithms like in Section 3.1.5. Regions of high uncertainty, e.g. outside of the validity range of the algorithms, should be masked.

3.4. Available software tools

Most research groups working with SAR wind retrieval are making their own software codes for internal use and algorithm development. For the regular user, only a few software tools are available for retrieval of wind from SAR imagery

The Next ESA SAR Toolbox (NEST, available from http://nest.array.ca/) is an open source toolbox for

reading, post-processing, analysing and visualising SAR data for most of the sensors relevant for wind retrieval. It is written in Java for portability, and has a plug-in functionality allowing users to develop (and share) their own modules. NEST is a general-purpose SAR analysis tool with presently only basic functionality for wind retrieval. Some research groups are using NEST for basic operations such as calibration, and perform wind retrieval with external software based on output from NEST.

SARTool is a commercial tool developed by CLS (formerly Boost Technologies), dedicated to SAR applications-based over the ocean and R&D activities. SARTool is the cornerstone of the operational activities conducted at VIGISAT (http://www.vigisat.eu/) such as CleanSeaNet 2 EMSA project or Soprano ESA project. SARTool has advanced wind retrieval functionality, including possibility for using several sources of external wind direction including manual ingestion for all the available SAR missions. Doppler shift or cross polarization can be used for wind inversion at C-band.

4. APPLICATIONS

4.1. Operational implementations

4.1.1. NOAA/NESDIS/STAR

For over a decade, NOAA ran a demonstration service that acquired RADARSAT-1 data and produced wind speed images in near real-time, leading to an operational service described in [84]. Among the lessons learned from this experience are the importance of accurate geolocation and calibration of the data. Near real-time availability makes the data most useful, and detailed data format documentation and sample source code to read the data encourages exploitation of the data and reduce errors in data application.

4.1.2. Soprano and French Marine Collaborative Ground Segment

Since 2007, working closely with ESA, CLS has shown that SAR data from ENVISAT could be acquired, archived, processed into wind field and delivered to users through a web portal in less than 15 minutes. This near real time service will be continued with Sentinel 1 A and B in the framework of the French Marine Collaborative Ground Segment (MCGS). This service will capitalize on the previous experience of Soprano (more than 60 000 ENVISAT products have been processed). In particular, attention will be paid to (i) the quality of the input level 1 product (calibration, noise equivalent sigma0, geolocation), (ii) the choice of the algorithms (Doppler and HV should be used to take benefit of these new capabilities) and (iii) the time and format to deliver the wind products. The MCGS will also allow massive reprocessing of data from different SAR missions given spatio-temporal criteria and selecting the most up-to-date algorithm. This reprocessing activity is mandatory to provide homogeneous dataset of wind measurements that can be used for wind farming or weather predictions applications as presented in sections 4.2 and 4.3.

4.2. Weather prediction

Due to limited spatial coverage and irregular revisit time of SAR sensors, SAR wind has hitherto hardly been used for operational weather forecasting, or for assimilation into numerical forecast models. However, several initiatives are emerging to demonstrate the potential benefit of using SAR winds in the field of weather forecasting.

Thanks to the success of the National SAR winds demonstration project (2009-2011), the operational production of SAR winds has been approved by Environment Canada (EC) and Meteorological Service Canada (MSC). The idea is to develop a chain able to provide wind information from SAR that can be directly included in the workstation used by forecasters [85]. This unique demonstration project has allowed collecting the feedback of many forecasters who have routinely compared their classical tools to the SAR observations. As reported in [86], the feedback is rather positive and SAR winds can benefit to forecasters [87].

Also, due to the recent abundance of SAR acquisitions, it is now possible to evidence systematic differences between high resolution SAR winds and low resolution numerical weather prediction model (such as ECMWF). In particular, for coastal areas, systematic biases occur with respect to the wind regime (speed and orientation of the mean flow with respect to the coast). If we assume that at first order, the topography of the coast drives most of the small physical processes (not resolved by low resolution models), then the systematic bias can be evaluated with respect to wind regime and accounted for to downscale the low resolution up to a 1 km wind field.

One method is to calculate SAR wind climatologies for a limited region, and to develop a transfer function (or "wind emulator") to relate this high resolution wind to some identifiable features of coarse scale numerical model wind fields. For future model predictions over the same area, where no SAR wind fields are available, the transfer function may then be applied to prescribe the finer scale winds "learned" from the SAR wind climatology. A preliminary study on this concept was performed by [88].

Another method is to use an "analogue" scheme. Recently, it has been shown such a method could be used to reduce systematic and random errors on the 10-

m wind speed predictions of WRF over land [89]. This methodology has been applied to the 10-m wind speed as given at low resolution by ECMWF to take into account for wind effects (observed and archived in a larger SAR dataset) that occur at high resolution in coastal area. As a result it is now possible to enrich on the fly the prediction from ECMWF in order to add the mean features that are expected at high resolution without having a SAR acquisition collocated in time and space. This has been applied off the coast of Tromsø and in Aegean Sea [90]. An example of ECMWF wind and its associated enriched high resolution wind field computed from a collection of SAR observations is presented on Figure 9.

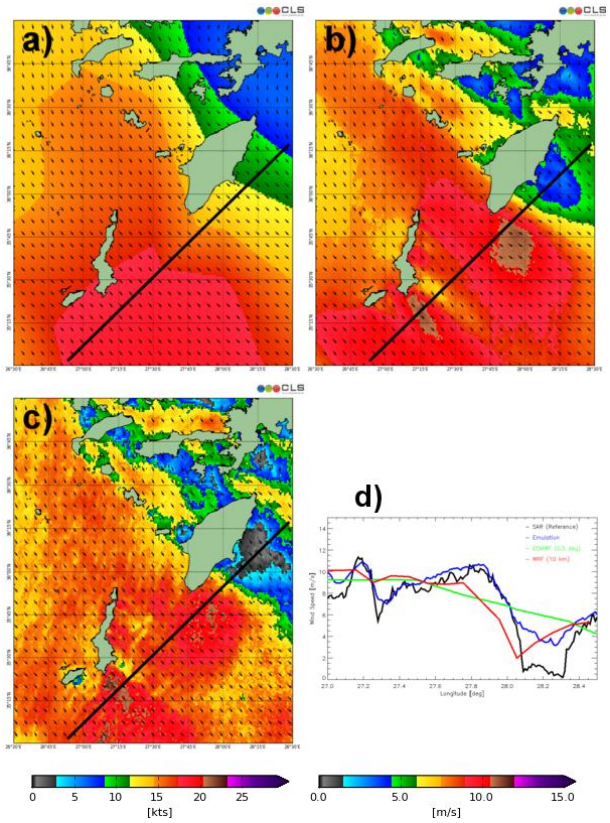

Figure 9: a) Wind field as given by ECMWF at a spatial resolution of 0.5°. b) Enriched ECMWF wind from high resolution learned from a collection of SAR winds acquired in the past. c) SAR Winds observed at the same time (not used for the enrichment) and used as reference. d) Transect to compare the ability of the wind emulator of [90] to capture the wind flow at high resolution. The green line is wind speed from ECMWF (fig a), red line is WRF (10 km resolution). The blue line is the emulated wind (fig b), and the black line is the reference SAR wind (fig c).

In both cases, this kind of exercise requires a large dataset of high resolution modelled and observed winds. Thanks to ENVISAT archive and RADARSAT-2 missions, since few years now, the archive of SAR images starts being interesting for such exercise. There is no doubt that the wind measurements of the forthcoming Sentinel-1 and RADARSAT Constellation missions will open new perspectives for this kind of applications.

4.3. Wind farming

Satellite SAR ocean wind maps are used for offshore wind farm projects characterizing winds in the coastal zone [91] and for wind resource assessment. Wind statistics such as mean wind speed, Weibull scale and shape parameters and energy density based on Envisat ASAR WSM wind maps compare well to high-quality offshore meteorological observations in the North Sea and Baltic Sea [92], [93] and there is good agreement in wind roses as seen in Figure 10.

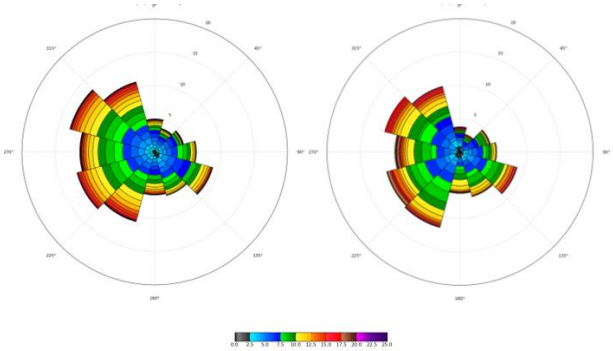

Figure 10: Wind roses from (left) mast at Horns Rev (M7) [7.9753°E ; 55.4873°N] and (right) all available Envisat ASAR WSM products [7.80°E ; 55.80°N].

Wind resource statistics for the Northern European Seas have been assessed from SAR winds level 2 products and the energy density map at 10 m (Figure 11) is published at www.norsewind.eu and soprano.cls.fr [94].

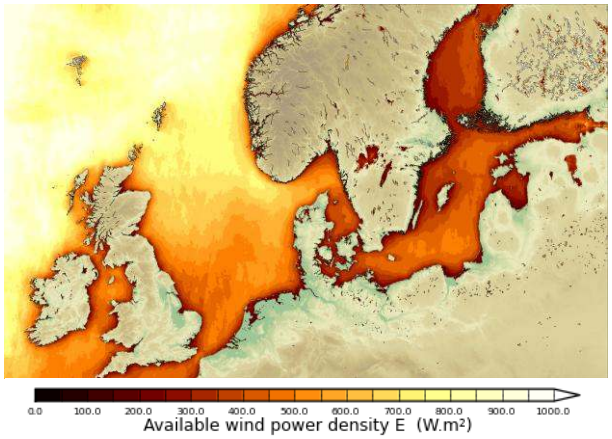

Figure 11: Wind energy density based on 9000 Envisat ASAR WSM scenes.

Research on methods to lift winds from 10 m to hub-height for wind resource assessment is on-going [95]. Another key topic is mapping wind farm wake [96], [97] where the reduced wind field, also called shadow effect, is quantified. Two examples of wind farm wakes detected by TerraSAR-X and RADARSAT-2 are shown in Figure 12 and Figure 13. High-resolution SAR is a unique source and gaining importance as offshore wind farm development grows in size and clusters of wind farms appear.

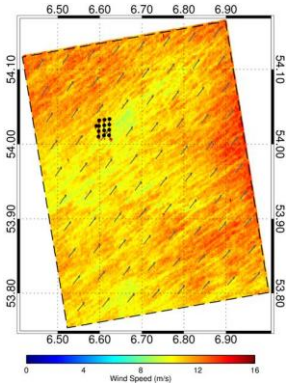

Figure 12: Wind wake induced by the Alpha Ventus wind farm in the North Sea, as observed with TerraSAR-X StripMap data at 2.5 m resolution.

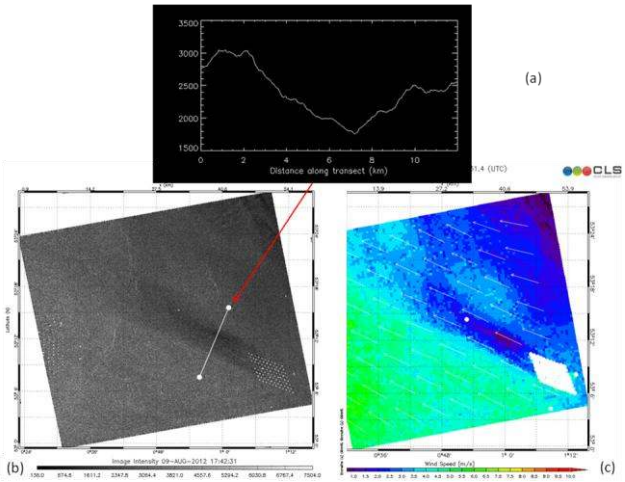

Figure 13: Signature of wind wake induced by wind farm as observed with a ScanSAR Wide RADARSAT-2. (a) Transect of measured intensity by SAR across the wind wake (b) Intensity image over Sheringham shoal wind farm in the North Sea. (c) Corresponding wind field estimated at 500 m resolution.

4.4. Process understanding

In addition to practical applications, SAR imagery has made invaluable contributions to the understanding of several mesoscale wind phenomena. Some examples are given in the subsections below.

4.4.1. Tropical cyclones

SAR data has been used to better understand the dynamics of tropical cyclone genesis, morphology and movement, because it can yield high-resolution (sub kilometer) and low-level storm information that cannot be seen below the clouds by other visible and infrared sensors. In addition to the wind field and tropical cyclone eye information, cyclone structures associated with atmospheric processes can also be detected by SAR. Recent studies shows that cyclone eye information (shape, size, etc.) can be quantitatively extracted from RADARSAT-1, RADARSAT-2 and Envisat SAR images [60], [98]. Different storm eye shapes are categorized, and it is found that stronger storms tend to be more symmetric in the eye shape. Examples of eye-eyewall, meso-vortices, rain bands and arc clouds are also clearly visible in SAR images. SAR cyclone observations also show a few unusual observations. One is that the storm pattern continues across the land-sea boundary. It is conjectured that this is due to rain scattering and attenuation in the atmosphere. The other one is that higher NRCS values are observed within some storm eyes which are usually believed to be a relatively calm area within the storm system. Possible explanations are rain, waves, and abnormally high wind. However, these phenomena cannot be addressed by SAR observation alone.

Although C-band is considered robust against atmospheric disturbances, a standard wind field retrieval technique using the scatterometer GMF CMOD5 often underestimates hurricane force winds. This could be explained by rain contamination and additional effects due to severe sea state that produce a strong damping of the NRCS. This leads, for wind speed above 20 m/s, to an error in the retrieved wind speed that is up to 30 m/s when using the standard procedure. Therefore, a new method to measure the hurricane intensity using SAR images, in combination with a parametric Holland-type model of wind speed, is introduced in [99]. Applied to five tropical cyclones, a good agreement is found, and wind speeds up to 70 m/s are determined with an RMS error of 3.9 m/s.

4.4.2. Polar lows

Polar lows are small atmospheric low pressure systems with a short lifetime of typically less than one day, developing over the ocean in polar regions in areas with strong temperature differences. Their small size (200-1000 km in horizontal scale) combined with few ground observations and radio soundings in the polar regions, are among the reasons why polar lows are seldom well predicted by numerical models.

SAR coverage has so far been too irregular for use in the forecasting, but several works have pointed to the

potential benefit of using SAR in the study and forecasting of polar lows [100], [101], [102]. Ref. [103] presented four case studies of polar lows in the Bering Sea, showing how SAR can lead to a better marine surface analysis, which is the basis for the forecast. Polar lows have been reported to be observed earlier in their development by the sea surface imprint in the SAR image, than by standard data [104]. Refs. [105] and [106] discuss the discontinuities in radar backscatter observed as spiraling lines towards the center of a polar low in the Labrador Sea. Ref. [107] investigated this case further using numerical model, and find that the discontinuities in the radar backscatter is due to wind shear and its impact on precipitation cells to be organized along the shear.

As numerical models are seldom correct due to time lag or misplacement of the location of the center, cross-polarisation data (as discussed in Section 3.1.2) is highly useful for wind retrieval in such highly variable situations as polar lows. All Envisat ASAR images of registered polar lows since 2002 over the Nordic Seas [108] have recently been collected in a database with other relevant data, to be used in further studies (http://polarlow.met.no/stars-dat).

4.4.3. Katabatic winds

A katabatic wind is a gravitational air flow that descends from a high-elevation mountain down slope to lower elevation. It usually occurs during night and early morning hours in the winter season when the air mass over the mountain top becomes colder and heavier due to fast radiation cooling and when the land-sea temperature gradient is large. Katabatic wind flow is forced by the mountain shape, and its velocity increases down slope. In coastal areas, the katabatic wind blows across the shoreline and leaves imprints on the sea surface. In literature [109], [110], SAR observations of the sea surface imprints of katabatic wind have been classified into three different types of patterns: 1) tongue-like; 2) mushroom-like; and 3) finger-like. SAR-derived wind associated with the katabatic wind varies between 5 and 8 m/s, and the katabatic wind pattern extends up to tens of km offshore. “Bora” is a special case of katabatic winds observed over the Adriatic Sea and also in the Black Sea, and have been studied using SAR e.g. by [111] and [138].

4.4.4. Gap winds

Gap winds are low level winds that may be intense and generally develop from orographic pressure gradients. Gap winds have been studied extensively and are quite common throughout the world. For example, gap winds have been documented in the Gulfs of Tehuantepec, Papagayo, and Panama in Central America [112], [113], [114], [115]; Cook Inlet, Shelikof Strait, Prince William Sound, and the Aleutian Archipelago in Alaska [116], [117], [118], [119]; Juan de Fuca Strait in Washington [120], [121], [122]; Strait of Gibraltar in Europe [123], [124]; Howe Sound in British Columbia [125]; Cook Strait in New Zealand [126]; Adriatic Sea in Europe [111], [127], [128], [129], [130], [131], and in Japan [133], [134], [135], [136], [137].

These winds are typically characterized as accelerated (~10-30 m/s) and shallow (< 1km) with a wide range of widths (O 100 m to 10 km). Recently, SAR imagery was used to quantify gap wind scales such as jet spreading rate, velocity decay rate, and length at which a gap jet becomes fully developed or self-similar, over the open ocean. SAR data from the Philippine Archipelago was used to determine that most jets followed the defined power laws, in which the jet half-width increased and the centerline velocity decreased with downstream distance from the jet exit [132]. However, the SAR data also showed that there were distinct deviations from a two dimensional plane jet flow. Variations were attributed to varying wind regimes, island interactions, adjacent jets properties, and limited spreading.

4.4.5. Vortex streets

When air flows around an obstacle, such as a mountain or island, atmospheric vortex streets (AVS’s) can develop on the lee side of the obstacle under favorable conditions. The AVS pattern consists of a double row of counter rotating vortex-pairs shedding alternately near each edge of the obstacle. The surface wind field associated with an AVS can also modify the sea surface roughness, and be imaged by SAR. AVS is frequently observed by SAR in the Aleutian Islands, Alaska region where low-level wind blows strong against the volcanic islands [139], [143]. The AVS can extend to a few hundred km downstream and the SAR observed dynamical processes can be simulated with models.

4.4.6. Boundary layer rolls

In SAR images of tropical cyclones, [140] found organized bands, roughly aligned with the mean wind, of near-surface wind convergence at wavelengths on the order of 10 km. The patterns bear a lot of similarity to regular planetary boundary layer (PBL) rolls, but have very large aspect ratio (wavelength divided by PBL depth) on the order of 5 to 10, which remain to be explained.

Theory [141] and observations [142] shows that the high shear and strong surface buoyancy flux in tropical cyclone boundary layers are ideal habitats for the growth and maintenance of $O(1$ to 3 km) wavelength roll vortices. Structures at ~2.4 aspect ratio grow much faster than rolls at longer or shorter wavelengths.

However, [141] showed that a wide range of growing instabilities with wavelengths ranging from sub-km to *O*(10 km) are capable of forming finite amplitude rolls. In this single-wave theory, rolls with wavelengths significantly larger or smaller than the *O*(1-3 km) wavelengths would not survive the competition since the *O*(1-3 km) wavelength rolls will reach the nonlinear growth stage and dominate the modified mean flow before the longer or shorter wavelength modes exhibit significant nonlinear growth. In order to compete, the longer wavelength modes must get an injection of energy to kick start them into the nonlinear regime.

4.4.7. Atmospheric gravity waves

Over the ocean, the low-level wind associated with atmospheric gravity waves (AGW) modulates the sea surface capillary wave spectra, and thus, leaves an alternating bright-dark roughness pattern associated with the wave crest-trough on the sea surface. This roughness pattern can be imaged by spaceborne SAR through the Bragg resonant scattering mechanism. In the literature, the sea surface imprints of orographically generated AGW in transverse, diverging and upstream forms have all been studied using spaceborne SAR images in conjunction with theoretical and numerical models [144], [145], [147], [148]. In some cases it may be difficult to discriminate signatures of AGW from internal waves in the ocean. Some identified criteria for this discrimination are described in [146].

5. OUTLOOK

Several interesting advances of SAR wind retrieval methodologies have been demonstrated in the last decade, in particular related to utilization of the cross-polarized NRCS and the Doppler Centroid shift as complementary to the co-polarized NRCS. Nevertheless, application of SAR for wind retrieval may be considered as fairly mature and robust, and thus the largest expectations for the future are related to availability and utilization of SAR wind products.

There are five major sources of civilian SAR data that are expected to become available in the near future (Table 1): Sentinel-1 (2 satellites), RADARSAT Constellation (3 satellites), TerraSAR-X and Tandem-X series, Cosmo SkyMed (4 satellites) and ALOS (2 satellites). These systems span the range of traditional SAR frequencies and offer new imaging capabilities, as well as unprecedented coverage and timeliness through the multi-satellite constellations. The major challenge to the exploitation of these data may not be technical, but programmatic. For SAR imagery to be useful for wind field monitoring and climatology, it will have to be available in large quantities and relatively inexpensively. The expensive per image model appropriate for some land applications will cause those interested in wind measurements to eschew data sources employing that model. However, with the unrestricted access to future Sentinel-1 data, it can be expected that some SAR imagery will also be provided freely by other agencies.

Unlike previous research-driven SAR systems, another new aspect of Sentinel-1 is acquisition of data in a semi-static pattern, so that the same areas are imaged in similar modes on a regular basis. It is up to the wind measurement community to encourage ESA to design the coverage pattern to aid wind measurement in coastal areas where SAR high-resolution wind fields are most useful. As with all other SAR-satellites, wind retrieval over coastal areas is limited by conflicting interests of land applications based on other imaging modes. This is particularly the case for the land-prioritized satellites TerraSAR-X and ALOS, but the modes favorable for wind retrieval should be encouraged as X- and L-band are shown to make a very interesting complement to the C-band systems. Generally for wind retrieval, VV polarization is preferred over HH, as the GMFs are better understood and the signals are stronger. Cross-polarized NRCS and Doppler anomaly grids have been demonstrated to be useful complements to co-polarized NRCS, and their availability and accurate calibration is encouraged. Wider swaths give generally better coverage still at a sufficient spatial resolution; though for case studies the high resolution modes with less spatial coverage may sometimes still be preferred.

Although there are great expectations in regard to future SAR sensors and missions, the existing archives of SAR imagery are far from fully utilized. In particular the historical wide swath imagery from Envisat and RADARSAT provide an excellent basis for both enlightening case studies as well for studying the statistics of various offshore mesoscale wind phenomena. This potential may even be enlarged by reprocessing historical data with improved calibration. One example is the Doppler Centroid grid from Envisat image which has been available only since 2007, and based on reverse-engineering post processing of the data [3]. The Doppler retrieval method by [150] is shown to provide both higher accuracy and better spatial resolution, and thus reprocessing of the full 10 year archive of Envisat ASAR wide swath imagery with this algorithm and improved noise level estimation would increase the value of this dataset for accurate retrieval of wind, as well as of waves and ocean surface currents.

Retrieval of wind, waves and currents from SAR should be regarded as closely coupled tasks. Nevertheless, retrieval of either parameter has traditionally been performed independently, by either neglecting or introducing simple corrections for the other two phenomena. As one example, the NRCS relates more

closely to the wind relative to the moving ocean surface, rather than the absolute wind speed. Thus, prevailing ocean currents show up as biases in scatterometer wind fields [151], and are also visible in the average SAR wind energy potential of Figure 11. Concurrent and consistent retrieval of wind, waves and surface currents is therefore a highly relevant and challenging future task [152], which would need a sophisticated combination of the SAR observables (Section 2.1), physical and empirical models (Sections 2.2 and 2.3) as well as auxiliary data sources. Constructs like polarization ratio and polarization difference are also likely to be useful for this task, as demonstrated by [153].

Acknowledgement
See the referenced papers for acknowledgements relating to support and collaborations of the co-authors. The views, opinions, and findings contained in this paper are those of the authors and should not be construed as an official National Oceanic and Atmospheric Administration or U.S. Government position, policy, or decision. This review paper is dedicated to the memory of Donald R. Thompson, who passed away in 2011. Don made numerous contributions to this field, and is remembered for his enthusiastic, generous, collaborative spirit.

6. REFERENCES

1. Monaldo F., Kerbaol V., Clemente-Colon P., Furevik B., Horstmann J., Johannessen J., Li X., Pichel W., Sikora T., Thompson D., and Wackerman C. (2003), The SAR Measurements of Ocean Surface Winds : A White Paper for the 2nd Workshop on Coastal and Marine Applications of SAR, Longyearbyen, Spitsbergen, Norway, 8-12 September 2003, ESA SP-565
2. Chapron B., Collard F., and Ardhuin F., Direct measurements of ocean surface velocity from space: Interpretation and validation, (2005). J. Geophys. Res. Oceans, vol. 110, no. C7, p. C07008.
3. Hansen, MW, Collard, F, Dagestad, K-F, Johannessen JA., Fabry P., Chapron B. (2011), Retrieval of Sea Surface Range Doppler Velocities from Envisat ASAR Doppler Centroid Measurements. IEEE Transactions on Geoscience and Remote Sensing. Vol.: 49. No.: 10, p.: 11
4. Mouche A, Collard F, Chapron B, Dagestad K-F, Guitton G, Johannessen JA, Kerbaol V, Hansen MW (2012). On the use of Doppler shift for sea surface wind retrieval from SAR. IEEE Transactions on Geoscience and Remote Sensing, Vol. 50, No. 7, pp 2901-2909
5. Madsen S. N. (1989), Estimating the Doppler Centroid of SAR Data. IEEE Transactions on Aerospace and Electronic Systems, Vol 25(2), pp 134-140
6. Vachon P.W., Dobson F.W., 1996, Validation of Wind Vector Retrieval from ERS-1 SAR Images over the Ocean, Global Atmos. Ocean Syst., vol. 5, pp. 177–187.
7. Wackerman C.C., Pichel W.G., Clemente-Colon P., (2003), Automated estimation of wind vectors from SAR, In: Proc. 83rd AMS Annual Meeting, LongBeach, CA.
8. Gerling, T. W., Structure of the surface wind field from the SEASAT SAR, J. Geophys. Res., vol. 91, 2308-2320, 1986.
9. S. Lehner, J. Horstmann and W. Koch (1998), Mesoscale wind measurements using recalibrated ERS SAR images, J. Geophys. Res., vol. 103, no. C4, 7847-7856, 1998.
10. Wackerman C.C., 2000, Estimating wind vectors from RADARSAT synthetic aperture radar imagery, Tech. Rep. 10032100-1-T, Veridian ERIM International, P.O. Box 134008, Ann Arbor, MI 48113-4008.
11. Du Y., Vachon P.W., Wolf J., 2002, Wind direction estimation from SAR images of the ocean using wavelet analysis, Canadian J. Remote Sens., vol. 28, pp. 498–509.
12. Fichaux N., Rachin T., 2002, Combined extraction of high spatial resolution wind speed and direction from SAR images: A new approach using wavelet transform, Canadian J. Remote Sens., vol. 28, pp. 510–516.
13. Horstmann J., Lehner S., Kock W., Tonboe R., (2000), Computation of wind vectors over the ocean using spaceborne synthetic aperture radar, The Johns Hopkins Univ. Tech. Dig., vol. 21, no. 1, pp. 100–107.
14. Horstmann, W. Koch, S. Lehner, and R. Tonboe, “Ocean winds from RADARSAT-1 ScanSAR”, *Can. J. Remote Sens.*, Vol. 28(3), pp. 524-533, 2002.
15. Wackerman, C.C., W.G. Pichel, and P. Clemente-Colon, ”A projection method for automatic estimation of wind vectors with RADARSAT SAR imagery”, *Proc. 2nd Workshop on Coastal and Marine Applications of SAR*, Svalbard, Norway, ESA SP-565, p. 55, 2003.
16. W. Koch, “Directional analysis of SAR images aiming at wind direction”, *IEEE Trans. Geosci. Remote Sensing*, DOI 10.1109/TGRS.2003.818811, Vol. 42, pp. 702-710, 2004.

17. J. Horstmann, and W. Koch, "Comparison of SAR wind field retrieval algorithms to a numerical model utilizing ENVISAT ASAR data", *IEEE Journal of Oceanic Engineering*, 30 (Iss.3), 508-515, doi 10.1109/JOE.2005.857514, 2005.
18. Wackerman C.C., Horstmann J., Koch W., Jul. (2003), Operational estimation of coastal wind vectors from RADARSAT SAR imagery, In: Proc. International Geoscience and Remote Sensing Symposium, Toulouse, France.
19. Elfouhaily, T., B. Chapron, K. Katsaros, and D. Vandemark (1997), A unified directional spectrum for long and short wind-driven waves, J. Geophys. Res., 102(C7), 15,781–15,796, doi:10.1029/97JC00467.
20. Kudryavtsev, V., Hauser, D., Caudal, G., and Chapron, B. (2003). A semiempirical model of the normalized radar cross-section of the sea surface 1. Background model. Journal of Geophysical Research (Oceans), 108:8054–+. doi: 10.1029/2001JC001003.
21. Bass, F. G., I. M. Fuks, A. I. Kalmykov, I. E. Ostrovsky, and A. D. Rosenberg, (1968), Very high frequency radiowave scattering by a disturbed sea surface, 2, Scattering from an actual sea surface, IEEE Trans. Antennas Propag., AP-16, 560 – 568
22. Valenzuela, G. R. (1978), Theories for the interaction of electromagnetic and ocean waves—A review, Boundary Layer Meteorol., 13, 61 – 85.
23. Plant, W. J., (1990), Bragg scattering of electromagnetic waves from the air/sea interface, in Surface Waves and Fluxes, vol. 2, Remote Sensing, pp. 41–108, Kluwer Acad., Norwell, Mass.
24. Phillips, O. M. (1988), Radar returns from the sea surface—Bragg scattering and breaking waves, J. Phys. Oceanogr., 18, 1063 – 1074.
25. Wright, J. W. (1968), A new model for sea clutter, IEEE Trans. Antennas Propag., AP-16, 217 – 223.
26. Romeiser, R., W. Alpers, and V. Wismann, An improved composite surface model for the radar backscattering cross section of the ocean surface, 1. Theory of the model and optimization / validation by scatterometer data, J. Geophys. Res., 102, 25,237-25,250, 1997.
27. Engen G., Pedersen I. F., Johnsen H., Elfouhailly T. (2006), Curvature Effects in Ocean Surface Scattering, IEEE Trans. on Antennas and Propagation, Vol.54, No.5, pp.1370-1379.
28. Mouche, A. A., B. Chapron, N. Reul, D. Hauser, and Y. Quilfen (2007), Importance of the sea surface curvature to interpret the normalized radar cross section, J. Geophys. Res., 112, C10002, doi:10.1029/2006JC004010.
29. Johannessen, J. A., B. Chapron, F. Collard, V. Kudryavtsev, A. Mouche, D. Akimov, and K.-F. Dagestad (2008), Direct ocean surface velocity measurements from space: Improved quantitative interpretation of Envisat ASAR observations, Geophys. Res. Lett., 35, L22608, doi:10.1029/2008GL035709.
30. Romeiser, R., and D.R. Thompson (2000), Numerical study on the along-track interferometric radar imaging mechanism of oceanic surface currents, IEEE Trans. on Geosci. and Remote Sensing, 38-II, 446-458.
31. Thompson, D.R. (1989), Calculation of microwave Doppler spectra from the ocean surface with a time-dependent composite model, in Radar Scattering from Modulated Wind Waves, edited by G.J. Komen and W.A. Oost, pp. 27-40, Kluwer Academic Publishers, Dordrecht, Netherlands.
32. Thompson, D. R., J. Horstmann, A. Mouche, N. S. Winstead, R. Sterner, and F. M. Monaldo (2012), Comparison of high-resolution wind fields extracted from TerraSAR-X SAR imagery with predictions from the WRF mesoscale model, J. Geophys. Res., 117, C02035, doi:10.1029/2011JC007526.
33. Attema E.P.W., (1986). An experimental campaign for the determination of the radar signature of the ocean at C-band. Proc. Third International Colloquium on Spectral Signatures of Objects in Remote Sensing, Les Arcs, France, ESA, SP-247, 791-799.
34. Cavani´ A., and D. Offiler, (1986). ERS-1 wind scatterometer: wind extraction and ambiguity removal. Proc. IGARSS 1986; Todays Solutions for Tomorrows Information Needs, Zurich, Switzerland, ESA SP-254, 395-398
35. Stoffelen, A. C. M., and D. L. T. Anderson, (1997). Scatterometer Data Interpretation: Derivation of the Transfer Function CMOD4, J. Geophys. Res., 102 (C3) 5,767-5,780.
36. Stoffelen, A. C. M., (1998). Error modeling and calibration; towards the true surface wind speed, J. Geophys. Res., 103, (C4) 7,755-7,766.
37. Monaldo F. M., Thompson D. R. (2006), Applicability of Conventional Scatterometer Model Functions to High-Resolution Wind Retrievals: the Effect of Spatial Averaging, Proceedings OceanSAR 2006 – Third Workshop on Coastal and Marine Applications of SAR, St. John's, NL, Canada, October 2006
38. Donnelly, W. J., Carswell J. R., McIntosh R. E., Chang P. S., Wilkerson J., Marks F., and P.

G. Black (1999). Revised Ocean Backscatter Models at C and Ku-band under High-wind Conditions, J. Geophys. Res., 104 (C5) 11,485-11,497.
39. Carswell, J. R., Castells A., Knapp E. J., Chang P. S., Black P. G. and F. Marks, (1999). Observed Saturation in C and Ku-band Ocean Backscatter at Hurricane Force Winds. Unpublished
40. Hersbach, H., A. Stoffelen and S. de Haan, An Improved C-band scatterometer ocean geophysical model function: CMOD5, J. Geophys. Res., 2007, 112, C03006, doi:10.1029/2006JC003743.
41. Quilfen, Y., B. Chapron, T. Elfouhaily, K. Katsaros, and J. Tournadre (1998), Observation of tropical cyclones by high-resolution scatterometry, J. Geophys. Res., 103(C4), 7767–7786, doi:10.1029/97JC01911.
42. Choisnard, J. and S. Laroche (2008), Properties of variational data assimilation for synthetic aperture radar wind retrieval, J. Geophys. Res., 113, C05006, doi:10.1029/2007JC004534.
43. Verhoef, A., M. Portabella, A. Stoffelen and H. Hersbach, CMOD5.n - the CMOD5 GMF for neutral winds, Document external project: 2008, SAF/OSI/CDOP/KNMI/TEC/TN/165, EUMETSAT, 2008. http://www.knmi.nl/publications/fulltexts/cmod5_neutral_winds_1.0.pdf
44. Portabella, M. and A.C.M. Stoffelen, On Scatterometer Ocean Stress J. Atm. Oceanic Technol., 2009, 26, 2, 368-382, doi:10.1175/2008JTECHO578.1.
45. Hersbach, Hans, 2010: Comparison of C-Band Scatterometer CMOD5.N Equivalent Neutral Winds with ECMWF. J. Atmos. Oceanic Technol., **27**, 721–736. doi: http://dx.doi.org/10.1175/2009JTECHO698.1
46. Thompson D. R., T. M. Elfouhaily, and B. Chapron (1998), Polarization ratio for microwave backscattering from the ocean surface at low to moderate incidence angles, in Proc. IGARSS, Seattle, WA, 1998.
47. Elfouhaily, T., S. Guignard, R. Awdallah, and D. Thompson (2003), Local and non-local curvature approximation: A new asymptottic theory for wave scattering, Waves Random Media, 13, 321– 337.
48. Zhang, B., W. Perrie, and Y. He (2011), Wind speed retrieval from RADARSAT-2 quad-polarization images using a new polarization ratio model, J. Geophys. Res., 116, C08008, doi:10.1029/2010JC006522.
49. Mouche, A., D. Hauser, J.-F. Daloze, and C. Guerin (2005), Dual-polarization measurements at C-band over the ocean: Results from ariborne radar observations and comparison with ENVISAT ASAR data, IEEE Trans. Geosci. Remote Sens., 43, 753–769.
50. Mouche, A. A., B. Chapron, and N. Reul (2007a), A simplified asymptotic theory for ocean surface electromagnetic wave scattering, Waves Random Complex Media, 17(3), 321–341.
51. Masuko, H., Okamoto, K., Shimada, M. and Niwa, S., (1986), Measurement of microwave backscattering signatures of the ocean surface using X band and Ka band airborne scatterometers. Journal of Geophysical Research, 91, pp. 13065–13083.
52. Ren, Y.-Z., Lehner, S., Brusch, S., Li, X.-M. and He, M.-X., (2012), An Algorithm for the retrieval of sea surface wind fields using X-band TerraSAR-X data. International Journal of Remote Sensing, 33, doi:10.1080/01431161.2012.685977.
53. Li, X.-M. and S. Lehner, (2012), Sea surface wind field by TerraSAR-X and Tandem-X data: algorithm development, submitted to IEEE TGARS.
54. Fu, L. L., and B. Holt, 1982: SEASAT views oceans and seas with synthetic aperture radar. Jet Propulsion Laboratory Publ. 81−102, Pasadena, CA, 200 pp.
55. Weissman, D. E., K, Davidson, R. Brown, C. Friehe, and F. Li, (1994), The relationship between the microwave radar cross section and both wind speed and stress: model function studies using Frontal Air-Sea Interaction Experiment data J, Geophys, Res,,Vol 99, C5
56. Shimada T., H. Kawamura, and M. Shimada, (2003), An L-band geophysical model function for SAR wind retrieval using JERS-1 SAR. In Proceedings of IEEE T. Geoscience and Remote Sensing, 518-531.
57. Isoguchi O. and M. Shimada, (2009), An L-band ocean geophysical model function derived from PALSAR, IEEE Trans. Geosci. Remote Sens., vol. 47, no. 7, pp. 1925–1936.
58. P. W. Vachon, and J. Wolfe, C-band cross-polarization wind speed retrieval, *IEEE Geosci. Remote Sens. Lett*., vol. 8, pp. 456-459, 2011.
59. P. A. Hwang, , B. Zhang, and W. Perrie, Depolarized radar return for breaking wave measurement and hurricane wind retrieval, *Geophys. Res. Lett*., vol. 37, L01604, doi:10.1029/2009GL041780, 2010.
60. B. Zhang and W. Perrie, Cross-polarized synthetic aperture radar: A new potential measurement technique for hurricanes, *Bull. Amer. Meteor. Soc.*, pp. 531-541, 2012.
61. Horstmann, J., S. Falchetti, S. Maresca, C. Wackerman, M. Caruso and H. Graber, “High

Resolution Tropical Cyclone Winds Retrieved from Satellite Borne C-band Cross Polarized Synthetic Aperture Radar", IEEE Trans. Geosci. Remote Sens., submitted 2012.

62. B. Zhang, W. Perrie, and Y. He, Wind speed retrieval from RADARSAT-2 quad-polarization images using a new polarization ratio model, *J. Geophys. Res.*, vol. 116, p. C08008, 8, 2011.
63. H. Shen, Y. He, and W. Perrie, Speed ambiguity in hurricane wind retrieval from SAR imagery, *International Journal of Remote Sensing*, vol. 30, pp. 2827–2836, doi:10.1080/01431160802555879, 2009.
64. H. Shen, W. Perrie, and Y. He., On SAR wind speed ambiguities and related geophysical model functions, *Canadian Journal of Remote Sensing*, vol. 35, no. 3, pp. 310-319, 10.5589/m09-012, 2009.
65. Luscombe, RADARSAT-2 polarimetric mode calibration and data quality assessment, *Proc. CEOS SAR Calibration and Validation Workshop*, Oberpfaffenhofen, Germany, 27-28 Nov. 2008.
66. Collard F., A. Mouche, B. Chapron, C. Danilo, and J. Johannessen, Routine high resolution observation of selected major surface currents from space, in Proc. SEASAR Symp., SP-656, ESA, ESA-ESRIN, Frascati, Italy, 2008.
67. Rouault M. J., A. Mouche, F. Collard, J. A. Johannessen, and B.Chapron, Mapping the Agulhas current from space: An assessment of ASAR surface current velocities, *J. Geophys. Res.*, vol. 115, p. C10026, Oct. 2010, doi:10.1029/2009JC006050.
68. Donelan, M. A., and W. J. Plant (2009), A threshold for wind-wave growth, J. Geophys. Res., 114, C07012, doi:10.1029/2008JC005238.
69. Foster, R., T. D. Sikora, and G. S. Young, (2004): The correction of surface layer wind speeds for atmospheric stratification and height. Proc. Second Workshop on Coastal and Marine Applications of SAR, Svalbard, Norway, 2003 September, European Space Agency SP-565, 39-47
70. He Y., Perrie, W., Q. Zou, and P. W. Vachon (2005), A new wind vector algorithm for C-band SAR, IEEE Trans. Geosci. Remote Sens., 43(7), 1453– 1458.
71. H. Shen, , W. Perrie, and Y. He, A new hurricane wind retrieval algorithm for SAR images, *Geophys. Res. Lett.,* vol. 33, L21812, doi:10.1029/2006GL027087, 2006.
72. Foster RC (2009), Boundary-layer similarity under an axi-symmetric, gradient wind vortex. *Bound.-Lay Meteorol*. 131 321-344.
73. Patoux, J Foster RC and RA Brown 2008: An evaluation of scatterometer-derived ocean surface pressure fields, *J Appl. Meteor. Clim*. 47, 835-853.
74. Patoux, J, RC Foster and RA Brown, 2011: Cross-validation of scatterometer measurements via sea-level pressure retrieval, submitted to *J Geo Phys. Res*.
75. Komarov S., Komarov A. And Zabeline V (2011), Marine wind speed retrieval from RADARSAT-2 dual-polarization imagery" Canadian Journal of Remote Sensing, 2011, 37(5): 520-528, 10.5589/m11-063.
76. Zhang, B., Perrie, W., Vachon, P. W., Li, X. and Pichel, W. G., 2012: Ocean vector winds retrieval from C-band fully polarimetric SAR measurements. *Trans. Geoscience and Remote Sensing.* In press. DOI 10.1109/TGRS.2012.2194157. 10 pages.
77. Portabella, M., A. Stoffelen and J.A. Johannessen (2002), Toward an optimal inversion method for SAR wind retrieval, J. Geophys. Res., 2002, 107, 8, doi:10.1029/2001JC000925
78. Yang, X., X. Li, W. G. Pichel and Z. Li, Comparison of ocean surface winds from Envisat ASAR, Metop ASCAT scatterometer, buoy measurements and NOGAPS model, IEEE Transactions on Geoscience and Remote Sensing, doi: 10.1109/TGRS.2011.2159802, 2011.
79. Yang, X., X. Li, Q. Zheng, X. Gu, W. Pichel and Z. Li, Comparison of ocean surface winds retrieved from QuikSCAT scatterometer and RADARSAT-1 SAR in offshore waters of the US West Coast, IEEE Geoscience and Remote Sensing Letters, 99, 163-167, doi: 10.1109/LGRS.2010.2053345, 2010.
80. Wackerman C., Pichel W. G., Li X., Clemente-Colòn P., (2006), Estimation of surface winds from SAR using a projection algorithm, Proc. 14th AMS Conference on Interaction of the Sea and Atmosphere, February 2006.
81. Shimada M., (2007), Correction of the SCANSAR Scalloping, Proceedings of ISAP2007, Niigata, Japan
82. Romeiser, R., J. Horstmann, M.J. Caruso, and H.C. Graber, "A Descalloping Post-Processor for ScanSAR Images of Ocean Scenes", *IEEE Trans. Geosci. Remote Sens.*, in press 2012, IEEE
83. Mouche A., Collard F., Chapron B., Johannessen J.A. (2012), Doppler Centroid, Normalized Radar Cross Sections and Sea Surface Wind, Proceedings of SeaSAR 2012 Tromsø, Norway, this issue.

84. Pichel W., Monaldo F., Jackson C., Sapper J., Li X., Keegstra P. (2012), SAR-Derived High-Resolution Operational Wind Products within NOAA CoastWatch, Proceedings of SeaSAR 2012 Tromsø, Norway, this issue.
85. Khurshid S., Bradley D. and Manore M. (2012), National SAR wind Product – User Requirements Document, Meteorological Service of Canada, Environment Canada;
86. Fogarty C. (2010), Operational Evaluation of SAR winds for Weather Forecast Applications. 2nd NSWP annual Meeting Otawa, ON, Canada.
87. Chan, K., B. Snyder, L. Neil, (2010): Using SAR Winds to Evaluate Synoptic and Mesoscale Features in Forecast Operations. Extended Abstract, 17th Conference on Satellite Meteorology, Annapolis, MD, USA, Amer. Meteor. Soc., P9.17..
88. Dagestad K.-F., Hansen M.W., Johannessen J.A., Collard F, Mouche A. (2009), Development and validation of a SAR wind emulator, Final report for the ESA project SAR wind, waves and currents, ESRIN/CONTRACT NO 18709/05/I-LG
89. Delle Monache L., Nipen T., Liu Y, Roux G., Stull R. (2011), Kalman Filter and Analog Schemes to Postprocess Numerical Weather Predictions, Monthly Weather Review, vol. 139.
90. Collard F. (2012) Swell emulation in coastal zone. Proceedings of SeaSAR 2012 Tromsø, Norway, this issue.
91. Barthelmie, R., J. Badger, S. Pryor, C. B. Hasager, M. B. Christiansen and B. H. Jørgensen, Offshore coastal wind speed gradients: issues for the design and development of large offshore windfarms, Wind Engineering, 31(6), 369-382, 2007.
92. Badger, M., J. Badger, M. Nielsen, C. B. Hasager and A. Peña, Wind class sampling of satellite SAR imagery for offshore wind resource mapping, Journal of Applied Meteorology, 49(12), 2474-2491, 2010
93. Hasager, C. B., M. Badger, A. Peña, X. G. Larsén and F. Bingöl, SAR-Based Wind Resource Statistics in the Baltic Sea, Remote Sensing, 3(1), 117-144, 2011.
94. Hasager, C. B., M. Badger, A. Mouche, A. Stoffelen, M. L. Driesenaar, I. Karagali, F. Bingöl, A. Peña, P. Astrup, M. Nielsen, A. Hahmann, P. Costa, E. Berge, R.E. Bredesen (2012), Norsewind satellite wind climatology, pp. 1-67, DTU Wind Energy-E-0007(EN), 2012.
95. Badger, M., A. Peña, R. E. Bredesen, E. Berge, A. Hahmann, J. Badger, I. Karagali, C. B. Hasager and T. Mikkelsen, Bringing satellite winds to hub-height, EWEA2012 Proceedings, 2012
96. Christiansen, M. B. and C. B. Hasager, Wake effects of large offshore wind farms identified from satellite SAR, Remote Sensing of Environment, 98, 251-268, 2005.
97. Christiansen, M. B. and C. B. Hasager, Using airborne and satellite SAR for wake mapping offshore, Wind Energy, 9, 437-455, 2006.
98. Li, X., J. A. Zhang, X. Yang, W. G. Pichel, M. DeMaria, D. Long, and Z. Li, Tropical cyclone morphology from spaceborne synthetic aperture radar, Bulletin of the American Meteorological Society, doi:10.1175/BAMS-D-11-00211.1, 2012.
99. A. Reppucci, S. Lehner, J. Schulz-Stellenfleth and S. Bruch (2010), Tropical cylcone intensity estimated from wide-swath SAR images, IEEE Transactions on Geoscience and Remote Sensing, 48(4).
100. Vachon, Paris W., Paul Adlakha, Howard Edel, Michael Henschel, Bruce Ramsay, Dean Flett, Maria Rey, Gordon Staples, and Sylvia Thomas (2000), Canadian Progress Toward Marine and Coastal Applications of Synthetic Aperture Radar, Johns Hopkins APL Technical Digest, vol 21, no. 1, 2000.
101. Rasmussen, E. and J. Turner (editors), (2003), Polar lows: Mesoscale weather systems in the polar regions, Cambridge University Press, Apr 17, 2003, 624 pages.
102. Furevik, Birgitte Rugaard, Gunnar Noer, Johannes Röhrs, Harald Schyberg and Frank Tveter (2012) SAR imaging of polar lows, proceedings of the SeaSAR workshop 2012, Tromsø, Norway, this issue.
103. Sikora, Todd D., Karen S. Friedman, William G. Pichel and Pablo Clemente-Colon (2000), Synthetic Aperture Radar as a Tool for Investigating Polar Mesoscale Cyclones, Weather and forecasting, Vol 15, 745-758, December.
104. Friedman, Karen S., William G. Pichel, Pablo Clemente-Colon, and Xiaofeng Li, A Study of Polar Lows with Synthetic Aperture Radar and GOES Imagery, Geoscience and Remote Sensing Symposium, Hamburg, 1999. IGARSS '99 Proceedings.
105. Chunchuzov, I., P. W. Vachon and B. Ramsay (2000), Detection and characterization of mesoscale cyclones in RADARSAT Synthetic Aperture Radar images of the Labrador Sea, Canadian Journal of Remote Sens., 26, 213-30.
106. Moore, G. W. K. and P. W. Vachon (2002), A polar low over The Labrador Sea: Interactions with topography and an upper-level potential

vorticity anomaly, and an observation by RADARSAT-1 SAR, Geophys. Res. Lett., 29(16), 1773, doi:10.1029/2001GL014007.
107. Martin, R. and G. W. K. Moore (2006) Transition of a synoptic system to a polar low via interaction with the orography of Greenland, Tellus, 58A, 236–253, 2006
108. Noer, G., Ø. Saetra, T. Lien and Y. Gusdal, A climatological study of polar lows in the Nordic Seas, Quarterly Journal of the Royal Meteorological Society Q. J. R. Meteorol. Soc. 137: 1762–1772, October 2011 A.
109. Alpers, W., U. Pahl, and G. Gross, Katabatic wind fields in coastal areas studied by ERS-1 synthetic aperture radar imagery and numerical modeling, J. Geophys. Res., 103, 7875–7886, 1998.
110. Li, X., W. Zheng, W. G. Pichel, C-Z Zou, and P. Clemente-Colon, Coastal katabatic winds imaged by SAR, *Geophysical Research Letters*, 34, L03804, doi:10.1029/2006GL028055, 2007.
111. Alpers, W., A. Ivanov, and J. Horstmann, (2009), Observations of bora events over the Adriatic Sea and Black Sea by spaceborne synthetic aperture radar, Mon. Wea. Rev., 137(3), 1154-1165, DOI: 10.1175/2008MWR2563.1, 2009
112. Chelton, D. B., Freilich, M. H., & Esbensen, S. K. (2000). Satellite observations of the wind jets off the Pacifc coast of Central America. Part I: Case studies and statistical characteristics. Monthly Weather Review, 128, 1993-2018.
113. Liang, J. -H., McWilliams, J. C., & Gruber, N. (2009). High-frequency response of the ocean to mountain gap winds in the northeastern tropical Pacific. Journal of Geophysical Research, 114, doi:10.1029/2009JC005370.
114. Steenburgh, W. J., Schultz, D. M., & Colle, B. A. (1998). The structure and evolution of gap outflow over the Gulf of Tehuantepec, Mexico. Monthly Weather Review, 126, 2673-2691.
115. Trasviña, A., Barton, E. D., Brown, J., Velez, H. S., Kosro, P. M., & Smith, R. L. (1995). Offshore wind forcing in the Gulf of Tehuantepec, Mexico: The asymmetric circulation. Journal of Geophysical Research, 100, 20649-20663.
116. Pan, Feifei, Ronald B. Smith, (1999): Gap Winds and Wakes: SAR Observations and Numerical Simulations. J. Atmos. Sci., 56, 905–923. doi: http://dx.doi.org/10.1175/1520-0469(1999)056<0905:GWAWSO>2.0.CO;2
117. Lackmann, G. M., & Overland, J. E. (1989). Atmospheric structure and momentum balance during a gap-wind event in Shelikof Strait, Alaska. Monthly Weather Review, 117, 1817-1833.
118. Liu, H., Olsson, P. Q., & Volz, K. (2008). SAR observation and modeling of gap winds in the Prince William Sound of Alaska. Sensors, 8, 4894-4914.
119. Liu, H., Olsson, P. Q., Volz, K. P., & Yi, H. (2006). A climatology of mesoscale model simulated low-level wind jets over Cook Inlet and Shelikof Strait, Alaska. Estuarine, Coastal and Shelf Science, 70, 551-566.
120. Winstead, N. S., Colle, B., Bond, N., Young, G., Olson, J., Loescher, K., et al. (2006). Using SAR remote sensing, field observations, and models to better understand coastal flows in the Gulf of Alaska. Bulletin of the American Meteorological Society, 87, 787-800.
121. Colle, B. A., & Mass, C. F. (2000). High-resolution observations and numerical simulations of easterly gap flow through the Strait of Juan de Fuca on 9-10 December 1995. Monthly Weather Review, 128, 2398-2422.
122. Overland, J. E., & Walter, B. A. (1981). Gap winds in the Strait of Juan de Fuca. Monthly Weather Review, 109, 2221-2233. 12. Reed, T. R. (1931). Gap winds of the Strait of Juan de Fuca. Monthly Weather Review, 59, 373-376.
123. Dorman, C. E., Beardsley, R. C., & Limeburner, R. (1995). Winds in the Strait of Gibraltar. Quarterly Journal of the Royal Meteorological Society, 121, 1903-1921.
124. Scorer, R. S. (1952). Mountain-gap winds; a study of surface wind at Gibraltar. Quarterly Journal of the Royal Meteorological Society, 78, 53-61.
125. Jackson, P. L., & Steyn, D. G. (1994). Gap winds in a fjord. Part I: Observations and numerical simulation. Monthly Weather review, 122, 2645-2665.
126. Reid, S. (1996). Pressure gradients and winds in Cook Strait. Weather and Forecasting, 11, 476-488.
127. Gohm, A., & Mayr, G. J. (2005). Numerical and observational case-study of a deep Adriatic bora. Quarterly Journal of the Royal Meteorological Society, 131, 1363-392.
128. Gohm, A., Mayr, G. J., Fix, A., & Giez, A. (2008). On the onset of bora and the formation of rotors and jumps near a mountain gap. Quarterly Journal of the Royal Meteorological Society, 134, 21-46.

129. Grubilic, V. (2004). Bora-driven potential vorticity banners over the Adriatic. Quarterly Journal of the Royal Meteorological Society, 130, 2571-2603.
130. Pullen, J., Doyle, J. D., Haack, T., Dorman, C., Signell, R. P., & Lee, C. M. (2007). Bora event variability and the role of air-sea feedback. Journal of Geophysical Research, 112, doi:10.1029/2006JC003726.
131. Smith, R. B. (1987). Aerial observations of the Yugoslavian bora. Journal of the Atmospheric Sciences, 44, 269-297.
132. Gierach, M. M., H. C. Graber, and M. J. Caruso, 2012: SAR-derived gap jet characteristics in the lee of the Philippine Archipelago. J. Remote Sens. Environ., 117, 289-300.
133. Yamaguchi, S. and H. Kawamura (2005), Influence of orographically steered winds on Mutsu Bay surface currents, J. Geophys. Res., 110, C09010, doi:10.1029/2004JC002462
134. Isoguchi O., T. Toyozumi, F. Sakaida, H. Kawamura (2006), Yamase-derived Gap Winds Off the Western Hokkaido Coasts and Their Effects on Sea Surface Temperature Fields. IGARSS 2006: 1655-1658
135. Shimada, T., M. Sawada, W.Sha, H. Kawamura, 2010: Low-Level Easterly Winds Blowing through the Tsugaru Strait, Japan. Part I: Case Study and Statistical Characteristics Based on Observations. *Mon. Wea. Rev.*, **138**, 3806–3821. doi: http://dx.doi.org/10.1175/2010MWR3354.1
136. Shimada, T., 2010: Structures and Seasonal Variations of Surface Winds Blowing through the Tsushima Strait. *J. Appl. Meteor. Climatol.*, **49**, 1714–1727. doi: http://dx.doi.org/10.1175/2010JAMC2301.1
137. Shimada, T. and Kawamura, H. (2011), Summertime gap winds of the Soya Strait induced by the developed Okhotsk high. Atmosph. Sci. Lett., 12: 316–320. doi: 10.1002/asl.345
138. Alpers, W., A. Yu. Ivanov, and K.-F. Dagestad (2011), Encounter of foehn wind with an atmospheric eddy over the Black Sea as observed by the synthetic aperture radar onboard Envisat, Mon. Wea. Rev., 139, 3992-4000, doi:10.1175/MWR-D-11-00074.1, 2011
139. Li, X., P. Clemente-Colon, W. G. Pichel and P. W. Vachon, Atmospheric vortex streets on a RADARSAT SAR image, *Geophysical Research Letters*, Vol. 27, No. 11, 1655-1658, 2000.
140. Foster R., (2012), Organized Multi-Km Surface Stress Convergence Lines in Tropical Cyclone Surface Wind Retrievals, Proceedings of SeaSAR 2012 Tromsø, Norway, this issue.
141. Foster, R. C., 2005: Why rolls are prevalent in the hurricane boundary layer. *J. Atmos. Sci*., **62**:2647–2661.
142. Morrison, I., S. Businger, F. Marks, P. Dodge, and J. A. Businger, 2005: An observational case for the prevalence of roll vortices in the hurricane boundary layer. *J. Atmos. Sci*., **62**:2662–2673.
143. Li, X.,W. Zheng, C-Z Zou, W. G. Pichel, A SAR Observation and Numerical Study on Ocean Surface Imprints of Atmospheric Vortex Streets, *Sensors*, 8, 3321-3334; doi: 10.3390/s80533212008, 2008.
144. Vachon, P. W., O. M. Johannessen, and J. A. Johannessen (1994), An ERS-1 synthetic aperture radar image of atmospheric lee waves, J. Geophys. Res., 99, 22,483–22,490, doi:10.1029/94JC01392.
145. Cheng, C. M., and W. Alpers, (2010), Investigation of trapped atmospheric gravity waves over the South China Sea using Envisat synthetic aperture radar images, Int. J. Rem. Sens., 31(17-18), 4725-4743, 2010
146. Alpers, W., and W. Huang, (2011), On the discrimination of radar signatures of atmospheric gravity waves and oceanic internal waves on synthetic aperture radar images of the sea surface, IEEE Trans. Geosci. Rem. Sens., 49(3), 1114-1126, 2011
147. Li, X., C. Dong, P. Clemente-Colon, W. G. Pichel, and K. S. Friedman (2004), Synthetic aperture radar observation of the sea surface imprints of upstream atmospheric solitons generated by flow impeded by an island, J. Geophys. Res., 109, C02016, doi:10.1029/2003JC002168.
148. Li, X., W. Zheng, X. Yang, Z. Li and W. Pichel (2011), Sea surface imprints of coastal mountain lee waves imaged by SAR, Journal of Geophysical Research, doi:10.1029/2010JC006643, 2011.
149. Monaldo, F. M., D. R. Thompson, and M. B. Christiansen, Retrieval of wind speed using L-band synthetic aperture radar, Proceedings IGARSS 2007, Barcelona, Spain, 2007.
150. Johnsen H., Engen G. (2012), High precision Doppler frequency estimation for ocean applications, Proceedings of SeaSAR 2012 Tromsø, Norway, this issue.
151. Kelly, K. A., Dickinson S., Johnson G.C., (2005): Comparisons of Scatterometer and TAO Winds Reveal Time-Varying Surface Currents for the Tropical Pacific Ocean. J. Atmos. Oceanic Technol., 22, 735–745.

152. Chapron B., Kudryavtsev V., Collard F., Johannessen J.A., Mouche A.(2012), Towards consistent inversion of wind, waves and surface current from SAR, Proceedings of SeaSAR 2012 Tromsø, Norway, this issue.

153. Kudryavtsev V., Collard F., Myasoedov A., Chapron B., Johannessen J.A. (2012), Dual-Polarized SAR Imaging of Meso-Scale Currents, Proceedings of SeaSAR 2012 Tromsø, Norway, this issue.

Table 1: Some past, present and future SAR satellites relevant for retrieval of wind. See http://database.eohandbook.com/ for a more complete overview. The wavelengths for the radar bands are: X: 2.5-4 cm, C: 4-8 cm, S: 8-15 cm, L: 15-30 cm.

Satellite/Sensor	Agency/ country	Year of operation	Radar band	Available polarizations	Swath width (max)	Incidence angle range [degrees]
ERS-1 / SAR	ESA	1991-2000	C	VV	100 km	20-26
JERS-1 / SAR	Jaxa, Japan	1992-1998	L	HH	75 km	32-38
ERS-2 / SAR	ESA	1995-2011	C	VV	100 km	20-26
RADARSAT1	CSA, MDA, Canada	1995-	C	HH	500 km	10-59
Envisat / ASAR	ESA	2002-2012	C	VV, HH, HH+HV, VV+VH	420 km	15-47
ALOS / PALSAR (2 satellites)	Jaxa, Japan	2006-	L	Quad	350 km	8-60
RADARSAT2 (3 satellites)	CSA, MDA, Canada	2007-	C	Quad	500 km	10-59
Cosmo-SkyMed (4 satellites)	ASI, Italy	2007-	X	Quad	200 km	20-60
TerraSAR-X (close formation with TanDEM-X)	DLR, Germany	2007-	X	VV, HH, HH+HV, VV+VH	100 km	15-60
HJ-1C	CAST, China	(2012-)	S	VV	100 km	25-47
Sentinel-1 (2 satellites)	ESA	(2014-)	C	VV, HH, HH+HV, VV+VH	400 km	20-45